

Hypoxia inducible factor signaling in breast tumors controls spontaneous tumor dissemination in a site-specific manner

Vera M. Todd^{1,2}, Lawrence A. Vecchi III^{2,3}, Miranda E. Clements⁴, Katherine P. Snow^{2,5}, Cayla D. Ontko⁶, Lauren Himmel⁷, Christopher Pinelli⁷, Marjan Rafat⁷ & Rachele W. Johnson^{1,2,3}✉

Hypoxia is a common feature in tumors and induces signaling that promotes tumor cell survival, invasion, and metastasis, but the impact of hypoxia inducible factor (HIF) signaling in the primary tumor on dissemination to bone in particular remains unclear. To better understand the contributions of hypoxia inducible factor 1 alpha (HIF1 α), HIF2 α , and general HIF pathway activation in metastasis, we employ a PyMT-driven spontaneous murine mammary carcinoma model with mammary specific deletion of *Hif1 α* , *Hif2 α* , or von Hippel-Lindau factor (*Vhl*) using the Cre-lox system. Here we show that *Hif1 α* or *Hif2 α* deletion in the primary tumor decreases metastatic tumor burden in the bone marrow, while *Vhl* deletion increases bone tumor burden, as hypothesized. Unexpectedly, *Hif1 α* deletion increases metastatic tumor burden in the lung, while deletion of *Hif2 α* or *Vhl* does not affect pulmonary metastasis. Mice with *Hif1 α* deleted tumors also exhibit reduced bone volume as measured by micro computed tomography, suggesting that disruption of the osteogenic niche may be involved in the preference for lung dissemination observed in this group. Thus, we reveal that HIF signaling in breast tumors controls tumor dissemination in a site-specific manner.

¹Graduate Program in Cancer Biology, Vanderbilt University, Nashville, TN, USA. ²Vanderbilt Center for Bone Biology, Vanderbilt University, Nashville, TN, USA. ³Department of Medicine, Vanderbilt University Medical Center, Nashville, TN, USA. ⁴Tumor Microenvironment and Metastasis Section, Pediatric Oncology Branch, Center for Cancer Research, National Cancer Institute, National Institutes of Health, Bethesda, MD, USA. ⁵Department of Medicine, Health, and Society, Vanderbilt University, Nashville, TN, USA. ⁶Department of Molecular Physiology and Biophysics, Vanderbilt University, Nashville, TN, USA. ⁷Department of Pathology, Microbiology and Immunology, Vanderbilt University Medical Center, Nashville, TN, USA. ⁸Department of Chemical and Biomolecular Engineering, Vanderbilt University, Nashville, TN, USA. ✉email: rachele.johnson@vumc.org

Tumor cells frequently experience hypoxic conditions as the metabolic demands of the proliferating cells exceed the supply of oxygen and nutrients from the existing blood vessels. Cells must adapt to these stressful conditions by altering their metabolism and recruiting new blood vessels to increase oxygen supply¹. The activation of hypoxia-inducible factor (HIF) signaling triggers these transcriptomic adaptations in response to low oxygen levels. Under normoxic conditions, HIF 1 alpha (HIF1 α) and HIF2 α are hydroxylated by prolyl hydroxylation domain (PHD)-containing enzymes^{2–5}, which allows von Hippel-Lindau factor (VHL)⁶, an E3 ubiquitin ligase, to bind to and ubiquitinate HIF1 α and HIF2 α , marking them for proteasomal degradation^{7–9}. In hypoxic conditions, PHD enzymes are inactive, leading to the stabilization of the alpha subunits, which can then dimerize with HIF1 β and translocate to the nucleus^{10,11}. Once in the nucleus, the HIF1 and HIF2 complexes bind to hypoxia response elements in the promoters of hypoxia-responsive genes and act as transcription factors^{12–14}. HIF1 α drives the expression of genes such as vascular endothelial growth factor (VEGF) to stimulate angiogenesis^{15,16}, as well as glucose transporters, glycolytic enzymes, and lactose dehydrogenase A to shift the main energy source of the cell to glycolysis^{17–21}. HIF signaling also promotes tumor cell metastasis by driving the expression of genes that control epithelial-to-mesenchymal transition (EMT), invasion, and extracellular matrix composition^{22–24}. Furthermore, clinical evidence from breast cancer patients shows that high HIF1 α levels in primary tumors correlate with poor patient outcomes^{25–28}, and a hypoxic transcriptomic signature in tumor cells is associated with bone metastasis^{29,30}. As such, HIF inhibitors are an attractive therapeutic avenue and are currently in development and undergoing clinical trials³¹.

High breast cancer patient morbidity and mortality arises from metastatic dissemination of tumor cells from the primary site, which occurs early in tumor progression^{32,33}. Approximately 70% of breast cancer patients present with lung or bone metastases upon autopsy^{34,35}. Thus, there is an urgent need to identify the molecular factors that drive tumor dissemination to distant metastatic sites. Previous studies suggest that HIF1 α expression in breast cancer cells promotes lung dissemination in genetic models³⁶ and bone colonization and osteolysis following intracardiac or orthotopic inoculation of MDA-MB-231 human breast cancer cells^{37–39}. However, the comparative contributions of Hif1 α and Hif2 α on spontaneous bone dissemination are not well understood. Furthermore, dissemination patterns to bone and lung, the two leading sites of metastasis for breast cancer, have not been simultaneously evaluated in a spontaneous metastasis model to the best of our knowledge. We therefore generated three transgenic mouse models of spontaneous mouse mammary carcinoma with tumor-specific deletion of *Hif1 α* , *Hif2 α* , and *Vhl* and evaluated the effects of HIF modulation on tumor dissemination to multiple distant sites using highly sensitive detection techniques that have been optimized to detect low levels of disseminated tumor burden⁴⁰. We found that deletion of *Hif1 α* or *Hif2 α* decreased dissemination to bone, while *Vhl* deletion increased bone dissemination. In contrast, *Hif1 α* deletion increased lung metastatic tumor burden while *Hif2 α* or *Vhl* deletion had no effect on lung dissemination. Thus, this study highlights the ability of HIF signaling to differentially modulate metastasis to certain sites.

Results

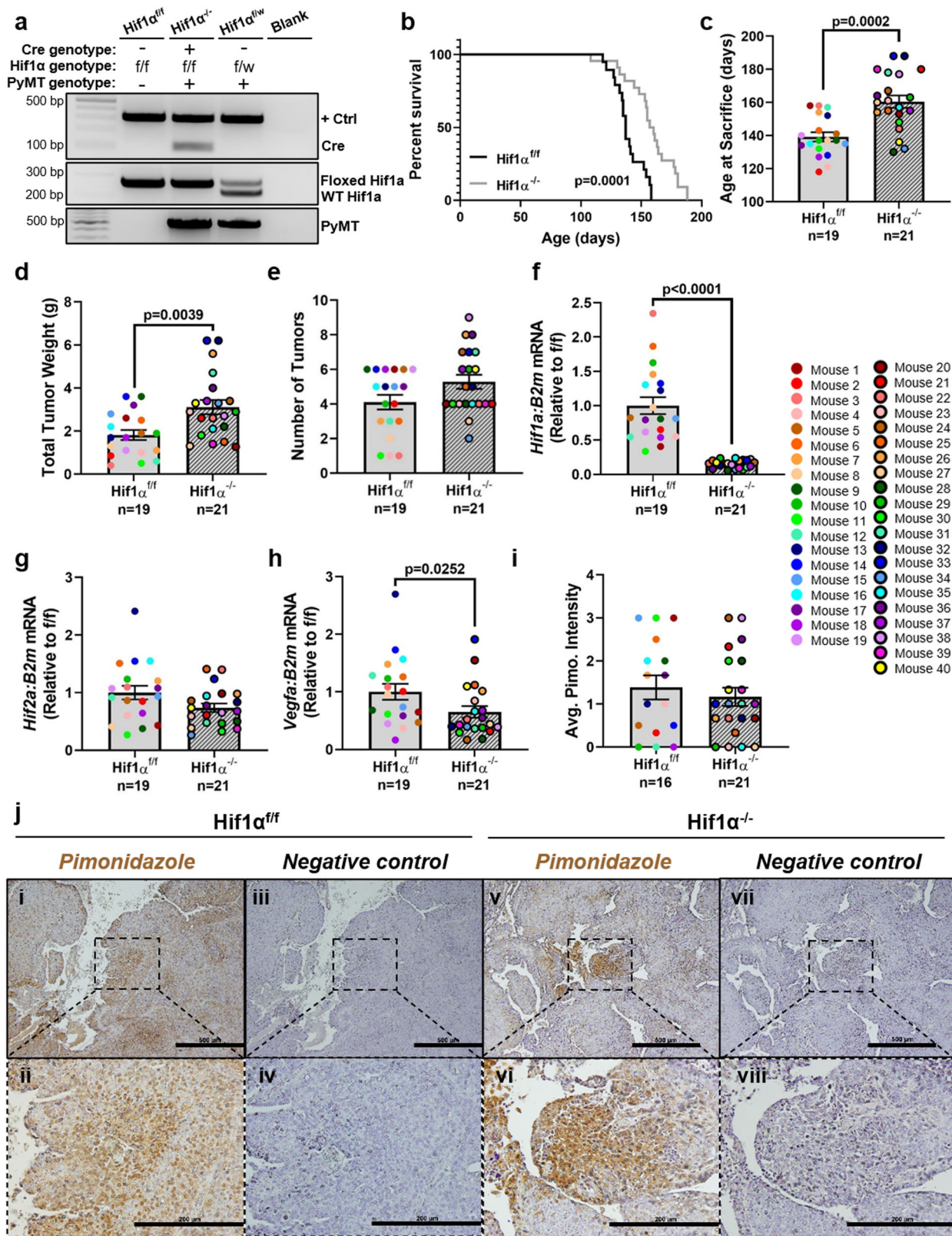
Deletion of *Hif1 α* increases total tumor burden while slowing primary tumor growth. To assess the impact of primary tumor HIF1 α expression on breast tumor cell dissemination to the bone, we generated an immune-competent spontaneous murine

mammary carcinoma model with mammary-specific deletion of *Hif1 α* using the Cre-lox system. In this model, mammary tumors grow spontaneously, driven by the polyoma middle T antigen (PyMT) expressed under the mouse mammary tumor virus long terminal repeats (MMTV-LTR), which restricts the oncogene expression to the mammary epithelium. In this study, we compared female *Hif1 α ^{-/-}* PyMT⁺ mice (*Hif1 α ^{fl/fl}*, Cre-positive, PyMT-positive) to control *Hif1 α ^{fl/fl}* PyMT⁺ mice (*Hif1 α ^{fl/fl}*, Cre-negative, PyMT-positive) (Fig. 1a). In this spontaneous model, mammary tumors were first palpable around 8 weeks of age and reached end point (any tumor reaching 1 cm in diameter) around 20 weeks of age for the *Hif1 α ^{fl/fl}* PyMT⁺ mice, while the *Hif1 α ^{-/-}* PyMT⁺ mice took significantly longer to reach end point, at an average of 23 weeks of age (Fig. 1b, c). This is consistent with previous reports using this model³⁶. Interestingly, the total tumor weight was greater on average in *Hif1 α ^{-/-}* PyMT⁺ mice upon sacrifice (Fig. 1d), while the number of tumors per mouse was not significantly increased (Fig. 1e).

We confirmed through real-time quantitative polymerase chain reaction (PCR) analysis of tumor homogenate RNA that *Hif1 α ^{-/-}* tumors had significant deletion of *Hif1 α* (Fig. 1f), while transcript levels of *Hif2 α* , the other major HIF pathway signaling factor, was unaffected (Fig. 1g). Recombination and deletion of *Hif1 α* was further confirmed by PCR amplification of the *Hif1 α* locus (Supplementary Fig. 1a, b). *Hif1 α* and *Hif2 α* transcript levels were unaffected in the lung, suggesting that we did not have off-target editing in other soft tissue sites (Supplementary Fig. 1c, d). Furthermore, the expression of *Vegfa*, a downstream target of Hif1 α , was significantly lower in *Hif1 α ^{-/-}* tumors (Fig. 1h), while the staining intensity of pimonidazole, a hypoxia marker, was comparable in *Hif1 α ^{fl/fl}* and *Hif1 α ^{-/-}* tumors (Fig. 1i, j). This confirms that *Hif1 α ^{-/-}* tumors have a dampened hypoxia response despite experiencing similar levels of hypoxia as *Hif1 α ^{fl/fl}* tumors.

Deletion of *Hif1 α* in the mammary fat pad reduces trabecular bone volume. Since bone disseminated breast tumor cells can cause the formation of osteolytic lesions, we first assessed trabecular bone volume of tibiae from *Hif1 α ^{fl/fl}* PyMT⁺ and *Hif1 α ^{-/-}* PyMT⁺ mice by microcomputed tomography (microCT) as a readout of tumor-induced bone destruction. To ensure that *Hif1 α* deletion in the mammary fat pad did not alter baseline bone microarchitecture, we also scanned tibiae from non-tumor bearing controls (PyMT⁻) of each genotype. Bone volume and trabecular number were significantly decreased in *Hif1 α ^{-/-}* PyMT⁺ mice, with an accompanying increase in trabecular spacing (Fig. 2a–d), but bone volume was unaltered with *Hif1 α* deletion in PyMT⁻ mice, suggesting that the reduction in bone volume observed in *Hif1 α ^{-/-}* PyMT⁺ mice was due to tumor-induced osteolysis. *Hif1 α ^{-/-}* PyMT⁻ mice did exhibit a significant increase in trabecular thickness (Fig. 2e), but this may not be biologically significant given the absence of changes in any other structural parameters for bone. Surprisingly, we found no discernible tumor burden present in the bone marrow of *Hif1 α ^{-/-}* PyMT⁺ mice upon histological inspection by a certified veterinary pathologist, save in one mouse (Fig. 2f, g). Thus, *Hif1 α* deletion in the primary tumor decreases trabecular bone volume but does not drive the development of macroscopic or osteolytic lesions in the bone.

Deletion of *Hif1 α* decreases bone dissemination while increasing lung metastasis. Given the lack of macroscopic tumor lesions in the bone and the fact that the main site of metastasis for the PyMT-driven mammary carcinoma model is the lung rather than the bone marrow^{41,42}, we employed several sensitive



strategies to determine whether there were differences in tumor dissemination to bone. First, tumor cells were detected by flow cytometry of bone marrow from the tibiae and femora from *Hif1α^{fl/fl}* PyMT⁺ and *Hif1α^{-/-}* PyMT⁺ mice based on epithelial cell adhesion molecule (EpCAM) positivity. While some background EpCAM staining was detected in non-tumor-bearing

(PyMT⁻) bone marrow (Supplementary Fig. 2), a significant decrease in the number of EpCAM⁺ cells was detected in the bone marrow from *Hif1α^{-/-}* PyMT⁺ mice compared to *Hif1α^{fl/fl}* PyMT⁺ mice when normalized to total tumor weight at end point (Fig. 3a and Supplementary Fig. 3a). Second, the tumor-specific *Pymt* transcript was quantified from femur and spine

Fig. 1 Deletion of *Hif1 α* increases total tumor burden while slowing primary tumor growth. **a** Example genotyping gel of Cre, floxed *Hif1 α* , and PyMT from *Hif1 α ^{f/f} PyMT⁺*, *Hif1 α ^{-/-} PyMT⁺*, and *Hif1 α ^{f/w} PyMT⁻* mice. “+ Ctrl” product indicates an internal positive control. **b** Survival analysis of *Hif1 α ^{f/f} PyMT⁺* and *Hif1 α ^{-/-} PyMT⁺* mice where end point represents sacrifice due to tumor size reaching collection threshold. Log-rank test. **c–e** Comparison of the age at sacrifice, total tumor burden at sacrifice, and number of tumors collected per mouse. Two-tailed Mann–Whitney test. **f–h** Quantitative PCR analysis of *Hif1 α* , *Hif2 α* , and *Vegfa* expression compared to *B2m* from whole-tumor homogenate RNA. Expression is normalized to the mean of the f/f control group. Two-tailed Mann–Whitney test. **i** The average pimonidazole staining intensity for each mouse across multiple images from a single tumor. Two-tailed Mann–Whitney test. **j** Representative images of pimonidazole staining, taken with $\times 10$ and $\times 40$ objectives. The $\times 40$ field is denoted with a dashed box in the $\times 10$ view. Scale bars represent 500 μm in $\times 10$ fields, and 200 μm in $\times 40$ fields. Negative controls lacked the primary antibody incubation step. Graphs represent mean per group and error bars represent s.e.m. $n = 19$ (or 16 in **i**) *Hif1 α ^{f/f} PyMT⁺* mice and $n = 21$ *Hif1 α ^{-/-} PyMT⁺* mice.

homogenate RNA as a marker of tumor burden (Fig. 3b, c and Supplementary Fig. 3b, c). No significant difference in tumor burden was detected in the femur and spine of *Hif1 α ^{-/-} PyMT⁺* mice using this method. Taken together, these results suggest that *Hif1 α* in the primary tumor promotes tumor cell dissemination to the bone.

In addition to quantifying tumor burden in bone sites, we quantified tumor burden in the lung by histological inspection in order to confirm that *Hif1 α ^{-/-} PyMT⁺* mice had decreased tumor burden, as reported previously³⁶. Surprisingly, *Hif1 α ^{-/-} PyMT⁺* mice had a significant increase in the number of metastatic lesions in the lung (Fig. 3d and Supplementary Fig. 3d, e) and total metastatic lesion area (Fig. 3e and Supplementary Fig. 3f, g), regardless of whether the data were normalized to total tumor weight at end point, the mouse age at sacrifice, or left unnormalized. Individual lesion size was not significantly different between the two groups (Supplementary Fig. 3h), indicating that the increase in total tumor area is driven by the greater number of lesions. *Hif1 α ^{-/-} PyMT⁺* mice also had significantly greater incidence of pulmonary lesions compared to *Hif1 α ^{f/f} PyMT⁺* mice (Fig. 3f). A non-significant trend in increased tumor burden was observed in the contralateral lung of *Hif1 α ^{-/-} PyMT⁺* mice by *Pymt* transcript levels (Supplementary Fig. 3i, j). To determine whether the increased tumor burden in the lung was indicative of a global metastatic increase in soft tissue sites, tumor burden was also measured in the brain and liver. There was a non-significant trend toward a reduction in tumor burden in the brain by *Pymt* transcript levels in *Hif1 α ^{-/-} PyMT⁺* mice (Supplementary Fig. 3k, l), and no liver lesions were detected by histological analysis by a certified veterinary pathologist (Supplementary Fig. 3m). Thus, *Hif1 α* deletion in the primary tumor reduces bone dissemination but also specifically promotes lung metastasis.

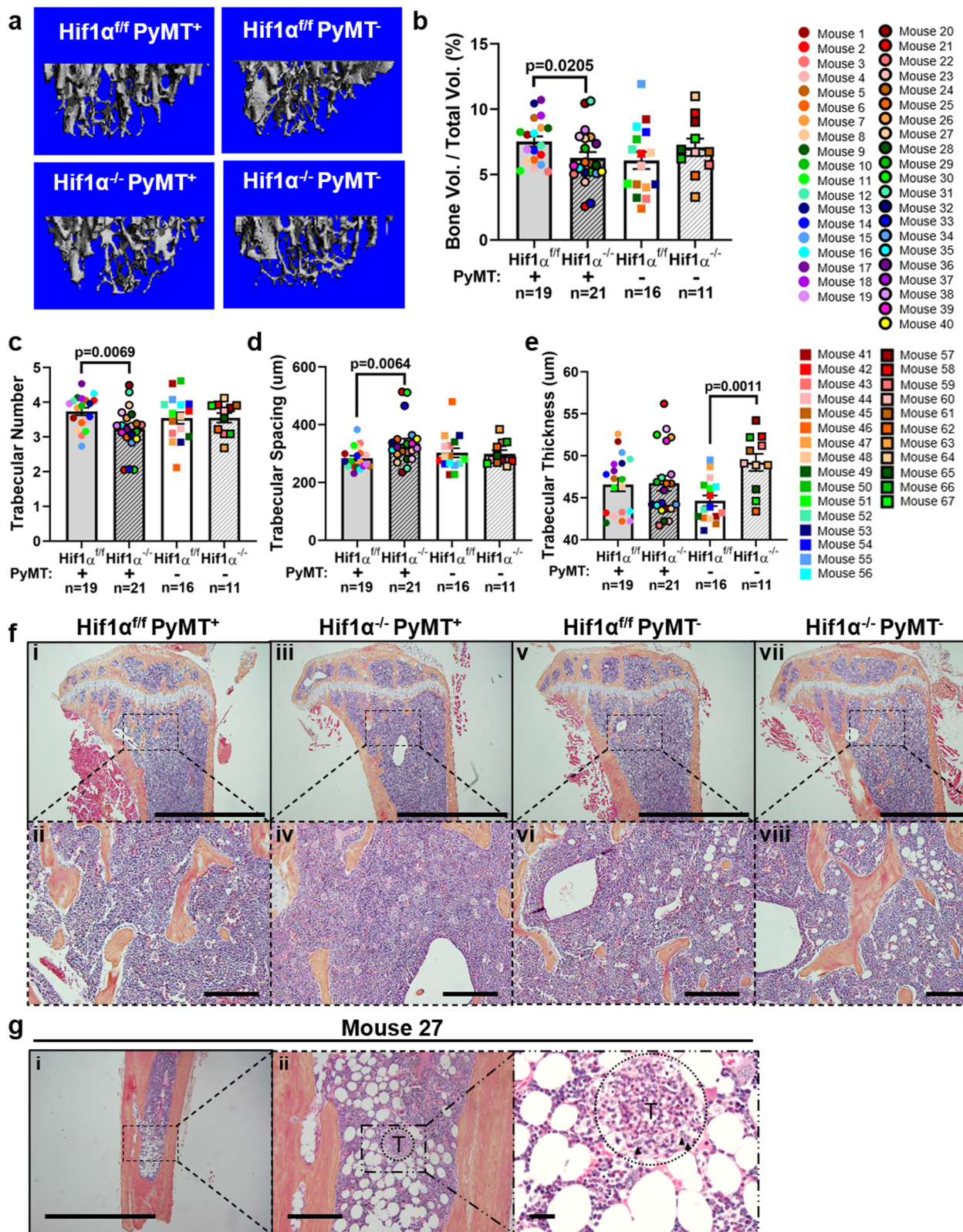
There was no difference in the expression of general breast cancer metastasis-associated genes (Fig. 4a), nor in EMT markers (Fig. 4b), between primary tumors from the *Hif1 α ^{f/f} PyMT⁺* and *Hif1 α ^{-/-} PyMT⁺* mice. This is consistent with site-specific differences in tumor burden, rather than a global increase or decrease in dissemination to all the distant sites measured. We also measured the expression of a panel of autophagy markers, since previous reports have shown that hypoxia-induced autophagy can affect pulmonary tumor burden. Inhibition of autophagy in hypoxic breast cancer cells has been shown to promote pulmonary metastasis⁴³, while autophagy has also been shown to promote the survival of dormant breast cancer cells and promote metastatic tumor recurrence⁴⁴. However, we saw no differences between *Hif1 α ^{f/f}* and *Hif1 α ^{-/-}* tumors in any of the autophagy markers tested (Fig. 4c).

We therefore examined gene expression data from The Cancer Genome Atlas (TCGA) Invasive Breast Carcinoma patient dataset to determine whether hypoxia differentially induced gene expression profiles associated with site-specific metastasis to the bone or lung. We found that a 42-gene hypoxia signature identified by Ye et al.⁴⁵ significantly and positively correlated with the bone metastasis signature established by Kang et al.⁴⁶

(Fig. 4d). Thus, hypoxia appears to drive a large transcriptomic program that promotes bone dissemination. However, a similar trend was observed for the lung metastasis signature from Minn et al.⁴⁷ (Fig. 4e). Taken together, it appears that hypoxia upregulates tumor dissemination in general at the transcriptomic level, suggesting that the increase in lung tumor burden may be due to altered *Hif1 α ^{-/-}* tumor cell response to signals from the lung microenvironment.

Proliferation and immune markers are unaltered in lung metastatic *Hif1 α ^{-/-} lesions.* To reconcile the divergent role of *Hif1 α* in tumor cell dissemination to bone and lung, we therefore sought to identify factors that may specifically be driving outgrowth of tumor cells in the lung. Since there is evidence that hypoxia promotes tumor dormancy specifically in the lung⁴⁸, we investigated whether the increased lung tumor burden in *Hif1 α ^{-/-} PyMT⁺* mice was due to dormancy escape by the lung-disseminated tumor cells. First, we confirmed that there was no significant difference in pimonidazole-positive lung lesion area, indicating that *Hif1 α ^{f/f}* and *Hif1 α ^{-/-}* tumor cells experience similar levels of hypoxia in the lung (Supplementary Fig. 4a, b). There was, however, no difference in Ki-67⁺ lung lesion area between the groups, indicating that *Hif1 α* expression does not alter the proliferative capacity of the disseminated cells once they exit dormancy (Fig. 4f, g). We next measured the abundance of CD4⁺ and CD8⁺ cells in the lungs, since altered immune cell numbers in the lung tissue may indicate differences in immune-mediated tumor cell clearance. However, there was no difference in CD4⁺ or CD8⁺ T cell infiltration in the lungs of *Hif1 α ^{f/f} PyMT⁺* and *Hif1 α ^{-/-} PyMT⁺* mice (Fig. 4h, i). Immune cell numbers were not significantly different between tumor-bearing lungs of *Hif1 α ^{f/f} PyMT⁺* and *Hif1 α ^{-/-} PyMT⁺* mice either (red points, Fig. 4h). To investigate whether pre-metastatic niche development could be driving the outgrowth of lung-disseminated tumor cells, we measured the expression of lysyl oxidase (LOX), a hypoxia-dependent tumor-secreted factor known to drive pre-metastatic niche development⁴⁹. However, there was no change in *Lox* expression between *Hif1 α ^{f/f}* and *Hif1 α ^{-/-}* tumors (Fig. 4j).

Deletion of *Hif2 α* decreases tumor dissemination to the bone but not to the lung. While *Hif1 α* and *Hif2 α* have some redundant functions, they have unique and sometimes opposing effects⁵⁰. To determine whether the dissemination patterns observed in the *Hif1 α ^{-/-} PyMT⁺* mice were due to a general decrease in HIF signaling activity, or due to *Hif1 α* -specific effects, we generated *Hif2 α ^{f/f} PyMT⁺* and *Hif2 α ^{-/-} PyMT⁺* mice using the same breeding strategy as the *Hif1 α ^{-/-} PyMT⁺* mice. We observed no difference between the *Hif2 α ^{f/f} PyMT⁺* and *Hif2 α ^{-/-} PyMT⁺* mice in the time it took tumors to reach collection size (Supplementary Fig. 5a, b), the total tumor weight upon sacrifice (Supplementary Fig. 5c), or the number of tumors (Supplementary Fig. 5d). We confirmed a significant reduction in *Hif2 α* transcript levels from whole-tumor homogenate RNA of *Hif2 α ^{-/-} PyMT⁺*



mice (Supplementary Fig. 5e) and no difference in *Hif1α* transcript levels (Supplementary Fig. 5f). *Hif2α* deletion did not significantly reduce *Vegfa* expression in the primary tumor (Supplementary Fig. 5g).

While microCT analysis of *Hif2α*^{-/-} PyMT⁺ mice did not reveal any differences in trabecular bone parameters (Supplementary Fig. 5h–l), flow cytometric analysis of hindlimb bone

marrow from *Hif2α*^{-/-} PyMT⁺ mice revealed a significant reduction in the percentage of EpCAM⁺ tumor cells (Fig. 5a). However, there was no significant difference in the *Pymt* transcript abundance in the femur or spine (Fig. 5b, c). Unlike the *Hif1α*^{-/-} PyMT⁺ mice, lung metastatic tumor burden in *Hif2α*^{-/-} PyMT⁺ mice was not significantly different than *Hif2α*^{fl/fl} PyMT⁺ mice, as measured by lesion number, total lesion

Fig. 2 Deletion of *Hif1α* in the mammary fat pad reduces trabecular bone volume. **a** Representative 3D renderings of microCT scans of the proximal metaphysis of the right tibia. **b–e** Quantification of bone volume as a percentage of total volume, trabecular number, trabecular spacing, and trabecular thickness. Two-tailed Mann-Whitney test against corresponding f/f control. **f** Representative H&E-stained images of the proximal metaphysis of the tibia taken with $\times 4$ and $\times 20$ objectives. The $\times 20$ field is denoted with a dashed box in the $\times 4$ view. Scale bars represent 2.0 mm in $\times 4$ view and 200 μm in the $\times 20$ view. **g** H&E-stained images of the one histologically detectable bone metastatic lesion, identified in the distal region of the tibia from Mouse 27. Lower-magnification images taken with $\times 4$ (i), $\times 20$ (ii) objectives, while highest magnification image (iii) is taken at $\times 600$ magnification. Scale bars represent 2.0 mm in $\times 4$ view, 200 μm in the $\times 20$ view, and 25 μm in $\times 600$ view. Area of higher magnification is indicated in lower magnification images with a dashed box. Tumor area is labeled T and indicated by dashed circle. Atypical cells denoted with arrowheads. Graphs represent mean per group and error bars represent s.e.m. $n = 19$ *Hif1α^{f/f}* PyMT⁺ mouse tibiae, $n = 21$ *Hif1α^{-/-}* PyMT⁺ mouse tibiae, $n = 16$ *Hif1α^{f/f}* PyMT⁻ mouse tibiae, and $n = 11$ *Hif1α^{-/-}* PyMT⁻ mouse tibiae.

area, individual lesion area, or incidence of lung metastases (Fig. 5d–g). Similarly, there was no significant difference in *Pymt* transcript abundance in the lungs or brains of *Hif2α^{-/-}* PyMT⁺ mice (Fig. 5h, i). Metastatic tumor burden data for *Hif2α^{-/-}* PyMT⁺ mice were un-normalized since there was no significant difference in tumor weight or age at sacrifice. Taken together, these results suggest that *Hif2α* in the primary tumor drives tumor cell dissemination to the bone but is dispensable for dissemination to the lung.

Deletion of *Vhl* increases tumor dissemination to the bone but not to the lung. To determine the effect of *Hif1α* and *Hif2α* activation, rather than deletion, we generated a third transgenic mouse strain in which we could model constitutive HIF signaling activation through deletion of *Vhl*, a negative regulator of HIF signaling. *Vhl^{f/f}* PyMT⁺ and *Vhl^{-/-}* PyMT⁺ mice were generated using the same strategy as the other transgenic strains. *Vhl^{-/-}* tumors took a significantly longer time to reach collection size compared to *Vhl^{f/f}* controls (Fig. 6a, b) but had a significant reduction in total tumor weight upon sacrifice (Fig. 6c). The average number of tumors was not significantly different between *Vhl^{f/f}* PyMT⁺ and *Vhl^{-/-}* PyMT⁺ mice (Fig. 6d). While we were unable to detect a decrease in *Vhl* transcript in whole tumor RNA from *Vhl^{-/-}* PyMT⁺ mice (Fig. 6e), we confirmed recombination of the *Vhl* locus at the genomic level (Fig. 6f) and observed a significant increase in the expression of *Vegfa*, phosphoglycerate kinase 1 (*Pgk1*), glucose transporter type 1 (*Glut1*), TEK receptor tyrosine kinase (*Tek*, also known as *Tie2*), and platelet-derived growth factor subunit B (*Pdgfb*) (Fig. 6g–k), indicating that HIF downstream signaling is elevated with *Vhl* deletion.

Despite unaltered trabecular bone parameters (Fig. 7a, b and Supplementary Fig. 7a–c), *Vhl* deletion increased the number of tumor cells detected in the bone marrow by flow cytometry when normalized to tumor weight (Fig. 7c and Supplementary Fig. 6d). No significant differences were observed in the *Pymt* transcript abundance in the femur or spine (Fig. 7d, e and Supplementary Fig. 6e, f). From histological analysis of the lung, no significant differences were observed in total metastatic lesion number or area between *Vhl^{f/f}* PyMT⁺ and *Vhl^{-/-}* PyMT⁺ mice, regardless of normalization to total primary tumor weight (Fig. 7f, g and Supplementary Fig. 6g, h). In addition, the incidence of lung metastases was no different between the two groups (Fig. 7h). There was a slight increase in the average individual lung lesion size in the *Vhl^{-/-}* PyMT⁺ mice (Supplementary Fig. 6i), but this difference was not sufficient to drive an increase in the overall lung tumor burden. Additionally, there were no significant differences in *Pymt* transcript abundance in the lungs or brains of *Vhl^{-/-}* PyMT⁺ mice (Fig. 7i, j and Supplementary Fig. 6j, k).

While *Hif1α* deletion was not found to alter the expression of genes involved in specific metastasis-related signaling pathways (Fig. 4), *Vhl* deletion was found to increase, although not significantly, the expression of *Pthlh* in the primary tumor (Fig. 8a). *PTH1H* and its gene product PTHrP are known to

promote breast tumor progression and metastasis⁵¹ and are key drivers of tumor-induced bone disease^{52–54}. Additionally, *PTH1H* is a direct target of HIF2α⁵⁵. Accordingly, we observed that *Hif2α*, but not *Hif1α*, deletion drove a modest, non-significant decrease in *Pthlh* expression (Fig. 8b, c). *Vhl* deletion also modestly increased the expression of *Cxcr4* (Fig. 8d), a gene known to drive breast cancer cell metastasis to bone^{56,57}, though this increase did not reach the threshold of statistical significance. *Hif1α* deletion did not result in a reciprocal decrease in *Cxcr4* expression, but *Hif2α* deletion yielded a non-significant decrease in *Cxcr4* (Fig. 8e, f). Due to the subtlety of expression changes observed for *Pthlh* and *Cxcr4*, other HIF-driven pro-metastatic factors are most likely involved in the mechanism behind HIF-driven bone metastasis (Fig. 8g).

Discussion

While our main analysis was focused on dissemination patterns and quantifying tumor burden in various distant sites, we observed surprising patterns in primary tumor growth. The slower tumor progression we observed in the *Hif1α^{-/-}* tumors has been reported previously in this model³⁶ and has been attributed to delayed microvessel growth in the mammary fat pad due to insufficient HIF signaling. Interestingly, while tumor progression is delayed, total tumor weight was higher on average in *Hif1α^{-/-}* PyMT⁺ mice than in *Hif1α^{f/f}* PyMT⁺ mice. However, in the previous study using this model³⁶, no significant difference in tumor weight at end point was noted. In contrast to *Hif1α*, our data indicate that *Hif2α* deletion does not significantly alter tumor progression, suggesting that HIF1α and HIF2α target distinct pathways that regulate tumor growth. Interestingly, while we expected *Vhl* deletion to yield the opposite tumor growth pattern from *Hif1α* deletion and cause tumors to grow more rapidly, *Vhl*-deleted tumors in fact progressed more slowly. *VHL* deletion has been reported to increase immune infiltration in mammary tumors⁵⁸, which may contribute to increased tumor cell clearance and the slower tumor growth and decreased total tumor weight observed in the *Vhl^{-/-}* PyMT⁺ mice.

Our finding that bone metastasis was significantly lower with *Hif1α* or *Hif2α* deletion are highly consistent with previous studies demonstrating that hypoxic signaling promotes tumor cell dissemination to the bone. HIF1α expression in breast cancer cells promotes bone colonization and osteolysis following intracardiac or orthotopic inoculation of MDA-MB-231 human breast cancer cells^{37–39}, and hypoxic transcriptomic signatures in breast cancer cells has been associated with bone metastasis^{29,30}.

It is important to note that our lung metastasis findings, which indicate that *Hif1α* inhibits lung metastasis while *Hif2α* has no effect, contradict a large body of work which demonstrates that both *Hif1α* and *Hif2α* promote lung metastasis. A prior study using the genetic MMTV-PyMT mouse model with mammary-specific deletion of *Hif1α* indicated that *Hif1α* expression promoted lung metastasis³⁶. The reason for the differences in our findings from previous studies are likely multifaceted. We used

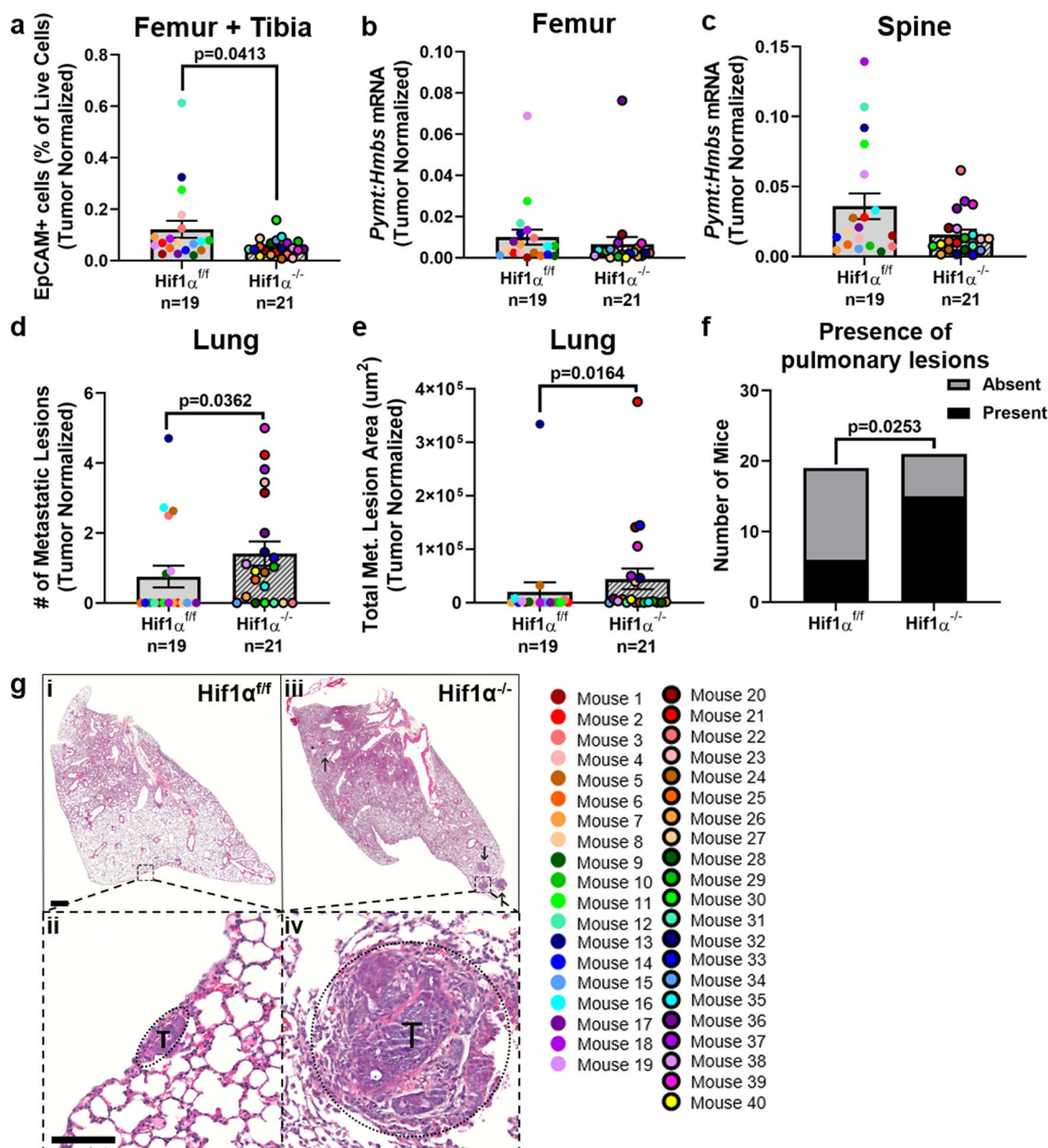
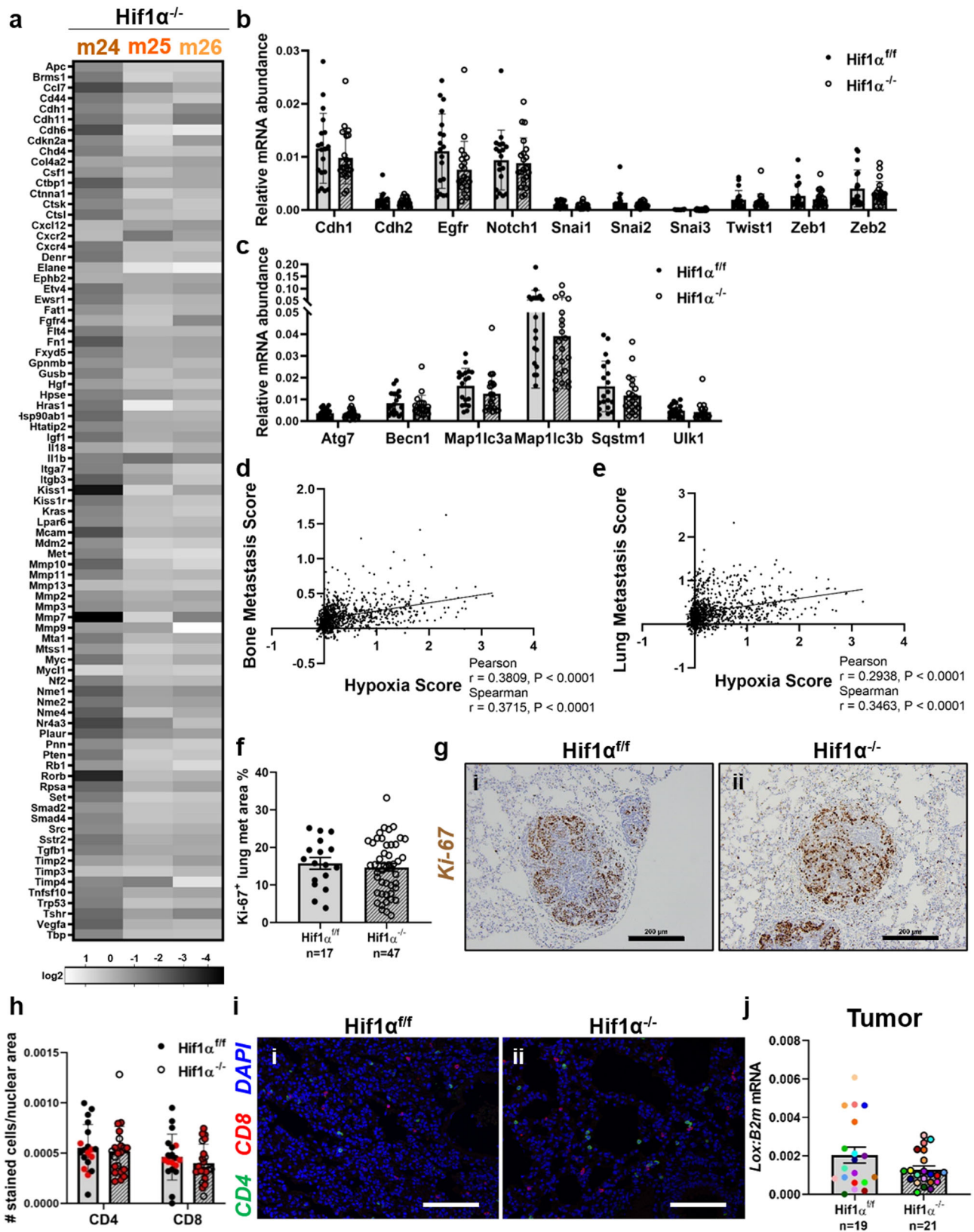


Fig. 3 Deletion of *Hif1 α* decreases bone dissemination while increasing lung metastasis. **a** The percentage of EpCAM⁺ cells, out of the total number of live cells, detected by flow cytometric analysis of left hindlimb bone marrow. Numbers are normalized to the total tumor weight of each mouse. Two-tailed Mann–Whitney test. **b, c** Quantitative PCR analysis of *Pymt* transcript compared to *Hmbs* from right femur or spinal midsection, respectively. *Pymt* expression was then normalized to the total tumor weight of each mouse. Two-tailed Mann–Whitney test. **d, e** Metastatic lesion number or area detected by histological analysis of H&E-stained sections from the left lung. Numbers are normalized to the total tumor weight of each mouse. Two-tailed Mann–Whitney test. **f** Comparison of the proportion of mice from each group that had any detectable pulmonary lesions. Fisher’s exact test. **g** Representative images of H&E-stained lung sections. Scale bar in sub-gross photomicrographs is 500 μ m. Scale bar in high-power micrographs is 100 μ m. The high-power image field is denoted with a dashed box in the sub-gross view. Tumor area is denoted with a dashed oval in the high-power images (labeled T). Additional metastatic lesions in the sub-gross view are denoted with arrows. Graphs represent mean per group and error bars represent s.e.m. $n = 19$ Hif1 $\alpha^{fl/fl}$ PyMT⁺ mice, $n = 21$ Hif1 $\alpha^{-/-}$ PyMT⁺ mice.

similar methodology, and we had a board-certified, blinded veterinary pathologist perform the lung tumor analysis. It is possible that the differences may be due to differences in genetic strain, since the combination of these mice is on a mixed genetic background. Our colony is therefore genetically distinct from the previous study. Significant differences have also been noted in microbiome composition of genetically engineered mice with the same genotype housed at different facilities⁵⁹. The commensal microbiota can significantly impact both local (gut) and systemic

immunity^{60,61} and thus could also influence the clearance or growth of disseminated tumor cells. Minor variations in animal handling and housing conditions, such as cage density and diet, have also been shown to affect biochemical, hematological, metabolic, and endocrine parameters⁶².

Additional studies similarly indicate that increased HIF signaling increases metastasis, including a 45-gene hypoxia response gene signature that was predictive of breast cancer patients’ risk of developing lung metastases³⁷. Several studies



using MDA-MB-231 human breast cancer cells or EMT6 murine mammary carcinoma cells have also demonstrated that inhibition of HIF1 α or HIF2 α significantly diminishes metastasis to the lung^{37,63,64}. HIF signaling has been shown to facilitate tumor cell extravasation by driving the expression of genes that increase breast cancer cell adhesion to endothelial

cells, such as L1 cell adhesion molecule, as well as genes that decrease adhesion between endothelial cells, such as angiopoietin-like 4⁶³. Specific downstream effectors of HIF signaling that prepare the lung microenvironment for metastatic colonization, such as LOX and LOX-like proteins (LOXL2 and LOXL4), have also been identified^{23,65}. A potential

Fig. 4 Hypoxia correlates with pro-metastatic transcription signatures. **a** Heatmap depiction of the expression of a panel of metastasis-associated genes from $n = 3$ $Hif1\alpha^{-/-}$ tumors compared to the average expression of $n = 3$ $Hif1\alpha^{+/f}$ tumors. The difference in expression of each gene between the three $Hif1\alpha^{+/f}$ and three $Hif1\alpha^{-/-}$ tumors was compared using the Mann-Whitney test. **b** Expression of a panel of EMT-related genes (*Cdh1*, *Cdh2*, *Egfr*, *Notch1*, *Snai1*, *Snai2*, *Snai3*, *Twist1*, *Zeb1*, *Zeb2*) compared to *B2m*, measured by qPCR. Two-tailed Mann-Whitney test against corresponding f/f control. **c** Expression of a panel of autophagy-related genes (*Atg7*, *Becn1*, *Map1lc3a*, *Map1lc3b*, *Sqstm1*, *Ulk1*) compared to *B2m*, measured by qPCR. Two-tailed Mann-Whitney test against corresponding f/f control. **d, e** Correlation of Ye et al. hypoxia gene signature⁴⁵ with mRNA levels of genes in the Kang et al. bone metastasis signature⁴⁶ or the Minn et al. lung metastasis signature⁴⁷, respectively, in TCGA Invasive Breast Carcinoma patient dataset. Pearson and Spearman correlation. $n = 1100$ patients. **f** Quantification of Ki-67⁺ area as a percentage of the lesion area. Two-tailed Mann-Whitney test. $n = 17$ individual $Hif1\alpha^{+/f}$ metastatic lung lesions, $n = 47$ individual $Hif1\alpha^{-/-}$ metastatic lung lesions. **g** Representative images of Ki-67-stained lung metastatic lesions, taken with $\times 20$ objective. Scale bars represent 200 μm . **h** Quantification of the average number of CD4⁺ and CD8⁺ cells in the lung normalized to the total nuclear area for the image. Data points in red denote mice that had detectable lung tumor burden. Two-tailed Mann-Whitney test against corresponding f/f control. **i** Representative images of immunofluorescent staining of CD4 and CD8, taken with $\times 20$ objective. Scale bars represent 200 μm . **j** Quantitative PCR analysis of *Lox* transcript compared to *B2m* from primary tumor homogenate RNA. Two-tailed Mann-Whitney test. Graph represents mean per group and error bars represent s.e.m. $n = 19$ $Hif1\alpha^{+/f}$ PyMT⁺ mice, $n = 21$ $Hif1\alpha^{-/-}$ PyMT⁺ mice.

explanation for the difference in findings from these prior studies may be due to our use of a spontaneous tumor formation and dissemination model since the majority of the previous studies utilized xenograft or syngeneic injection models, or may be due to differences between PyMT tumor cells and the tumor lines utilized in the other studies. It is possible that, since the PyMT-driven spontaneous mammary cancer model has such a robust lung metastasis phenotype, contributions of HIF signaling may be negligible. This would explain why we do not see changes in lung tumor burden in the *Hif2 α* - or *Vhl*-deletion models and could point to a yet unidentified mechanism at play in the *Hif1 α* -deletion strain that exhibited increased lung metastasis.

Thus far, we have not been able to identify a molecular driver for the increased lung metastasis observed with *Hif1 α* deletion and have eliminated a significant number of potential mechanisms. We demonstrated that *Hif1 α* expression does not alter the proliferative capacity of macroscopic lung lesions, but due to the collection time point we were not able to detect single disseminated tumor cells in these mice. As we collected mice relatively late in disease progression in order to maximize the amount of disseminated cells, the lung lesions were already well developed. Thus, we could not determine whether the proliferative capacity of these disseminated tumor cells was altered by *Hif1 α* expression prior to their development into histologically detectable lesions. We cannot rule out that disseminated tumor cells that had not yet grown into macroscopic lesions are detectable in mice collected earlier in disease progression and there may be differences in Ki-67 staining at that time point. Given the subtlety of our model and the large mouse numbers necessary for robust statistical analysis at earlier time points, it would be difficult to assess these differences earlier in the model. Importantly, normalizing lung tumor burden to age at sacrifice did not change our finding that *Hif1 α* deletion increased lung metastasis, indicating that our data is likely not an artifact of the difference in collection age.

Additionally, this difference in outgrowth of disseminated tumor cells could be due to tumor cell-intrinsic properties driven by *Hif1 α* expression or due to microenvironmental changes in the lung that result from *Hif1 α* expression in the primary tumor. First, alterations in immune cell populations in the lung may alter the outgrowth of lung metastatic cells due to immune-mediated tumor cell clearance⁶⁶. We measured the presence of CD4⁺ and CD8⁺ cells in the lungs of $Hif1\alpha^{+/f}$ PyMT⁺ and $Hif1\alpha^{-/-}$ PyMT⁺ mice but observed no differences. However, other immune cell types are also involved in tumor cell clearance. Modulating the activity or polarization of immune cells is also known to create microenvironments that oppose or support tumor growth. For example, T cell inactivation is known to create a permissive microenvironment for tumor growth⁶⁷, and tumor-associated

macrophages can promote tumor progression through many pathways, such as inducing tissue remodeling and fibrosis, taming of adaptive immunity, and providing protective niches for cancer stem cells⁶⁸. Some immune cell types, especially CD11b⁺ cells, have been implicated in the establishment of the pre-metastatic niche^{49,69} that fosters tumor cell growth. Thus, a more extensive immune cell profiling of the lung may reveal differences that would explain the difference in tumor cell outgrowth. Second, primary tumor-secreted factors have been shown to affect the establishment of a pre-metastatic niche. Hypoxia-induced LOX secretion from breast cancer cells is a driver of pre-metastatic niche development in the lung⁴⁹ as well as osteolytic lesion development in the bone^{29,70}. While we did not observe a difference in *Lox* expression that would explain the increased lung tumor burden and decreased bone volume observed in $Hif1\alpha^{-/-}$ PyMT⁺ mice, this is not the only factor that regulates pre-metastatic niche development. In prostate cancer, exosomes released from hypoxic cancer cells have been shown to promote matrix metalloproteinase activity at pre-metastatic sites⁷¹. The mechanisms that govern pre-metastatic niche development at various anatomical sites is not yet well characterized, and the impact of hypoxia on this process warrants further investigation.

Interestingly, a change in lung tumor burden was only observed in the *Hif1 α* -deleted mice, and not in the *Hif2 α* - or *Vhl*-deleted mice. Of note, a decrease in tibial bone volume was observed in the $Hif1\alpha^{-/-}$ PyMT⁺ mice, but not in the *Hif2 α* - or *Vhl*-deleted mice. The osteogenic niche is key to the establishment and growth of disseminated tumor cells in the bone marrow, as the interaction of tumor cells with osteoblast lineage cells through heterotypic adherens junctions activates pro-proliferation pathways⁷². However, osteoblast-secreted factors have also been shown to induce dormancy and quiescence in prostate cancer cells^{73,74}, indicating that the osteogenic niche can promote quiescence of tumor cells that engraft in these regions of the bone. Since the osteogenic niche is reduced in the $Hif1\alpha^{-/-}$ PyMT⁺ mice, as indicated by the reduction in bone volume, the shrinkage of suitable niches available for tumor cell engraftment in bone may cause a larger portion of the metastatic tumor cells to engraft in the lung instead. This may explain why we do not observe a difference in lung tumor burden in *Hif2 α* - or *Vhl*-deleted mice. The mechanism behind the decreased bone volume in $Hif1\alpha^{-/-}$ PyMT⁺ mice remains unclear; however, it is important to note that there was no difference in bone volume between $Hif1\alpha^{+/f}$ and $Hif1\alpha^{-/-}$ PyMT⁻ mice, suggesting that the reduction in bone volume is not due to deletion of *Hif1 α* in off-target cell lineages, but rather due to tumor-related factors.

While a loss of the osteogenic niche could explain the reduction in bone dissemination and increase in lung metastasis observed in the $Hif1\alpha^{-/-}$ PyMT⁺ mice, other mechanisms must

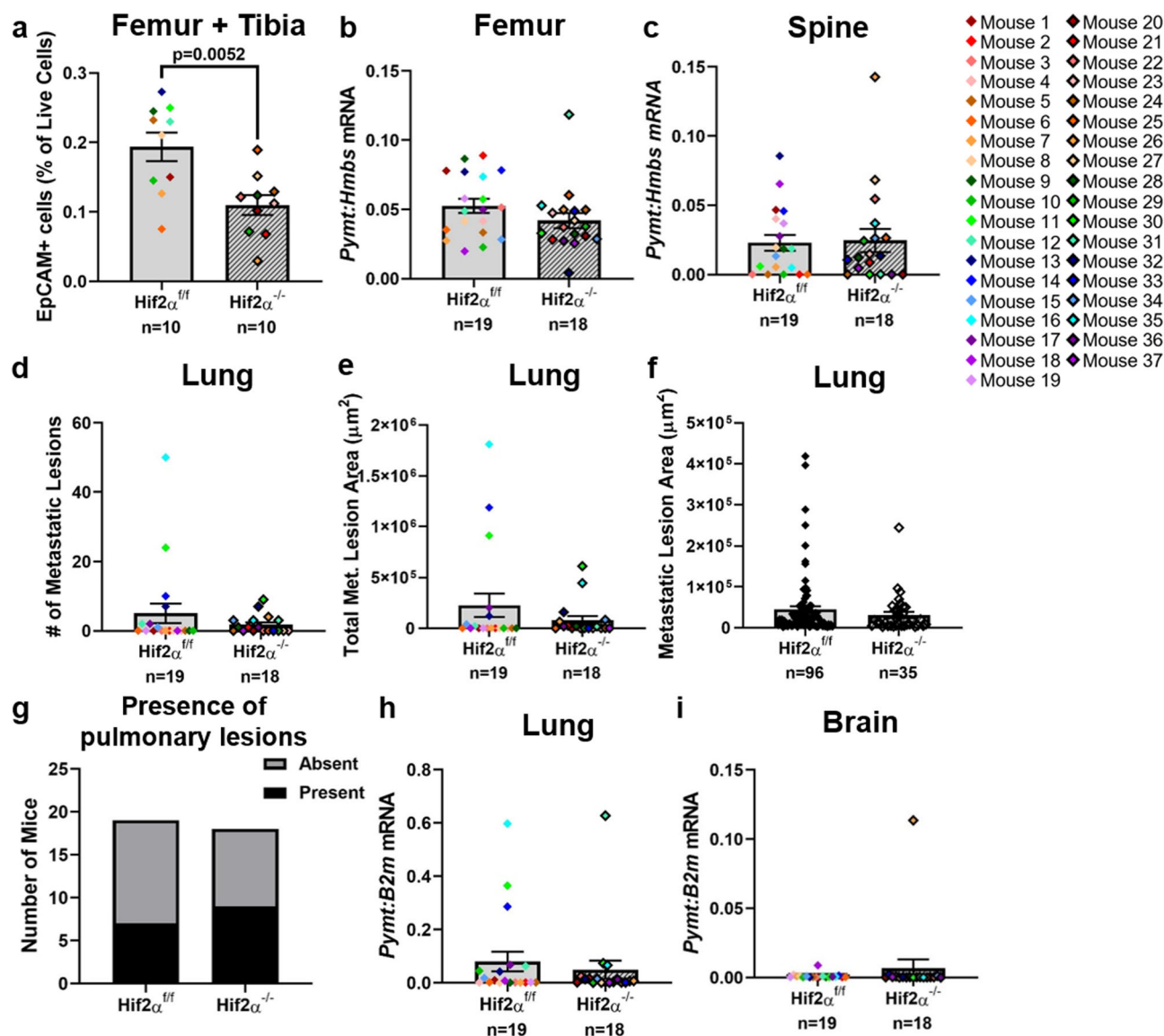


Fig. 5 Deletion of *Hif2α* decreases tumor dissemination to the bone but not to the lung. **a** The percentage of EpCAM⁺ cells, out of the total number of live cells, detected by flow cytometric analysis of left hindlimb bone marrow. Two-tailed Mann-Whitney test. $n = 10$ *Hif2α*^{fl/fl} PyMT⁺ or *Hif2α*^{-/-} PyMT⁺ mice. **b, c** Quantitative PCR analysis of *Pymt* transcript compared to *Hmbs* from right femur or spinal midsection, respectively. Two-tailed Mann-Whitney test. **d, e** Metastatic lesion number or area detected by histological analysis of H&E-stained sections from the left lung. Two-tailed Mann-Whitney test. **f** Comparison of individual lesion areas detected from histological inspection of left lung sections. Two-tailed Mann-Whitney test. $n = 96$ individual *Hif2α*^{fl/fl} metastatic lung lesions, $n = 35$ individual *Hif2α*^{-/-} metastatic lung lesions. **g** Comparison of the proportion of mice from each group that had any detectable pulmonary lesions. Fisher's exact test. **h, i** Quantitative PCR analysis of *Pymt* transcript compared to *B2m* from the right lung or brain, respectively. Two-tailed Mann-Whitney test. Graphs represent mean per group and error bars represent s.e.m. For **b-e, g-i**, $n = 19$ *Hif2α*^{fl/fl} PyMT⁺ mice, $n = 18$ *Hif2α*^{-/-} PyMT⁺ mice.

be involved in the bone dissemination phenotypes we observed in *Hif2α*^{-/-} PyMT⁺ and *Vhl*^{-/-} PyMT⁺ mice. Our data suggest that reduced expression of PTHrP in the primary tumor may, in part, mediate the decreased bone dissemination in *Hif2α*^{-/-} PyMT⁺ mice, while increased C-X-C chemokine motif receptor 4 (CXCR4) expression may be involved in the regulation of bone dissemination in *Vhl*^{-/-} PyMT⁺ mice, although it is important to note that neither gene was significantly changed. PTHrP (gene name *PTH1H*) is a key driver of osteolysis in bone-disseminated breast cancer, but its role in the primary tumor is more nuanced⁷⁵. Previous work using the MMTV-PyMT model demonstrated that PTHrP deletion in the mammary epithelium delays primary tumor initiation, inhibits tumor progression, and reduces metastasis to distal sites⁵¹. Loss of primary tumor PTHrP

expression in a MMTV-*neu* model of breast cancer, however, showed the opposite outcome, with PTHrP loss resulting in higher tumor incidence⁷⁶. Clinical studies have also shown that patients with PTHrP-positive primary tumors have significantly improved survival and fewer metastases to distant sites, including the bone^{77,78}. PTHrP is known to be expressed in a HIF2α, but not HIF1α, dependent manner⁵⁵. In accordance with the modest decrease in *Pthlh* expression we observe in *Hif2α*^{-/-} tumors, the trend toward increased *Pthlh* expression in *Vhl*^{-/-} tumors may be due to Hif2α activation rather than Hif1α. CXCR4 is known to drive breast cancer metastasis to bone through engagement with its cognate ligand, CXCL12, which is highly expressed on mesenchymal stromal cells in the bone marrow^{56,57}. Interestingly, although CXCR4 expression is known to be HIF1α dependent³⁹,

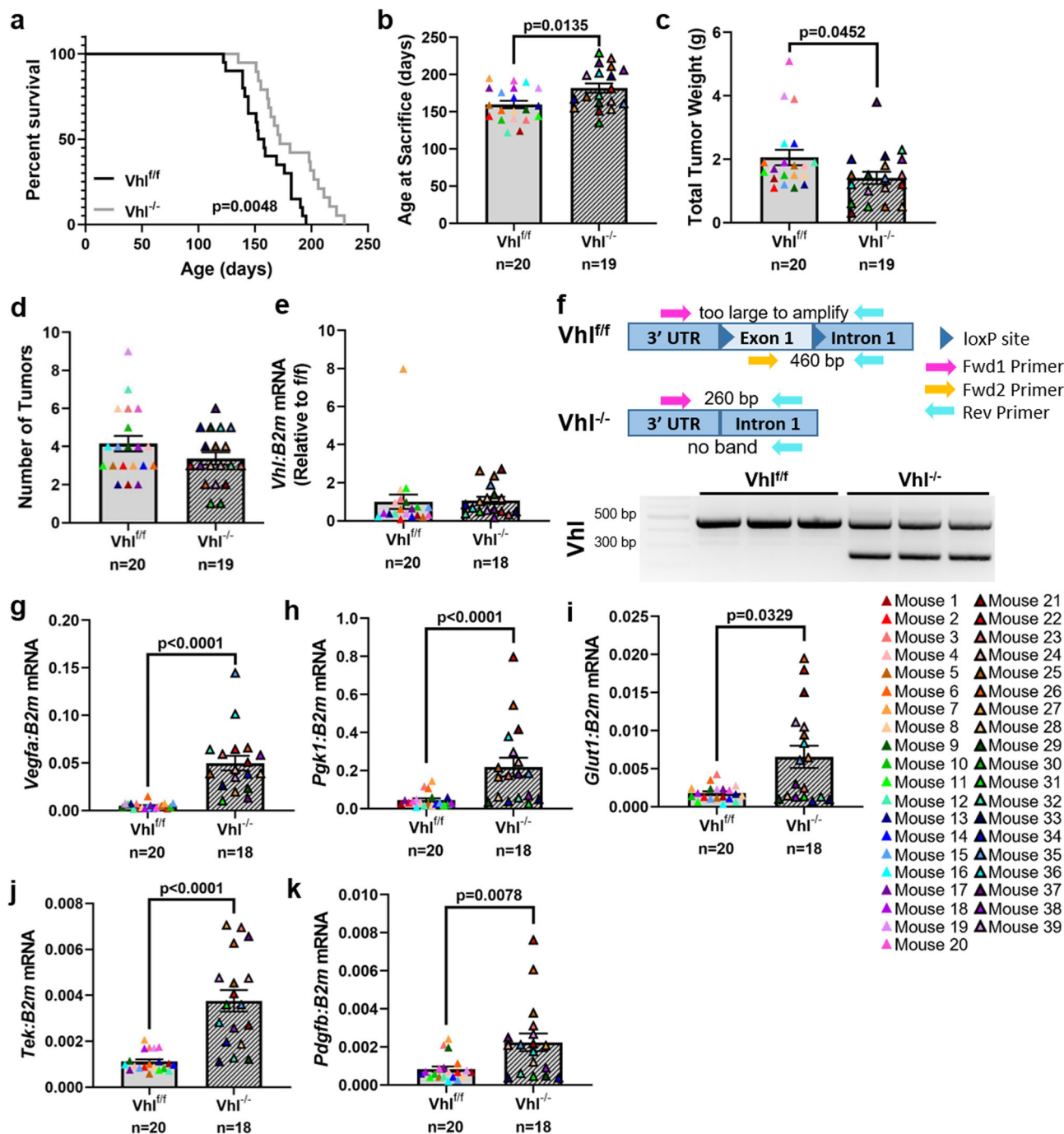


Fig. 6 Deletion of *Vhl* slows primary tumor growth and decreases total tumor burden. **a** Survival analysis of *Vhl*^{f/f} PyMT⁺ and *Vhl*^{-/-} PyMT⁺ mice where end point represents sacrifice due to tumor size reaching collection threshold. Log-rank test. **b–d** Comparison of the age at sacrifice, total burden at sacrifice, and number of tumors collected per mouse. Two-tailed Mann-Whitney test. **e** Quantitative PCR analysis of *Vhl* expression compared to *B2m* from whole-tumor homogenate RNA. Expression is normalized to the mean of the f/f control group. Two-tailed Mann-Whitney test. **f** Schematic of PCR-based validation of *Vhl* locus recombination using a three-primer PCR reaction. Genomic DNA was used as the input material. DNA electrophoresis gel represents the PCR products from the reactions depicted in the schematic diagram. The lower molecular weight of the band in the *Vhl*^{-/-} lanes indicate successful recombination. The residual band in the *Vhl*^{-/-} lanes are likely from non-recombined stromal cells present in the tumor. **g–k** Quantitative PCR analysis of HIF target genes (*Vegfa*, *Pdgfr1*, *Glut1*, *Tek*, *Pdgfb*) compared to *B2m* from whole-tumor homogenate RNA. Two-tailed Mann-Whitney test. Graphs represent mean per group and error bars represent s.e.m. *n* = 20 *Vhl*^{f/f} PyMT⁺ mice, *n* = 19 (or 18 in **e–k**) *Vhl*^{-/-} PyMT⁺ mice.

we did not observe a decrease in *Cxcr4* transcript in response to *Hif1a* deletion. There is also evidence that *Hif2a* is required for CXCR4 expression in renal cancer cell lines⁷⁹, but we did not observe a significant difference in *Cxcr4* expression in response to *Hif2a* deletion. This suggests that, in our model, deletion of either

of the HIFα factors on their own was not sufficient to decrease *Cxcr4*, but the combined stabilization of *Hif1a* and *Hif2a* may have been sufficient to drive *Cxcr4* expression. Alternatively, the modest increase in *Cxcr4* in response to *Vhl* deletion could be mediated by HIF-independent pathways. While VHL functions to

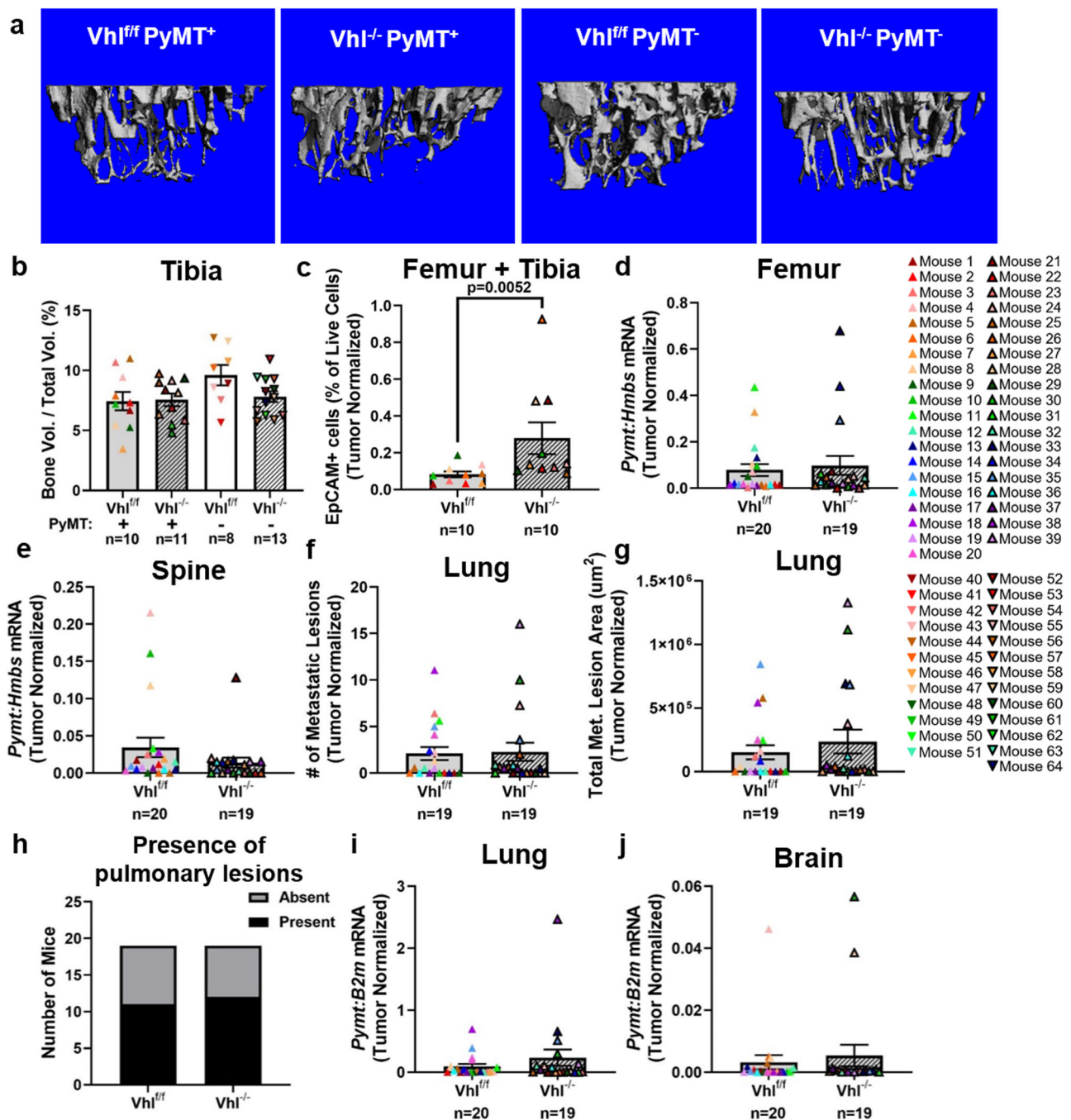
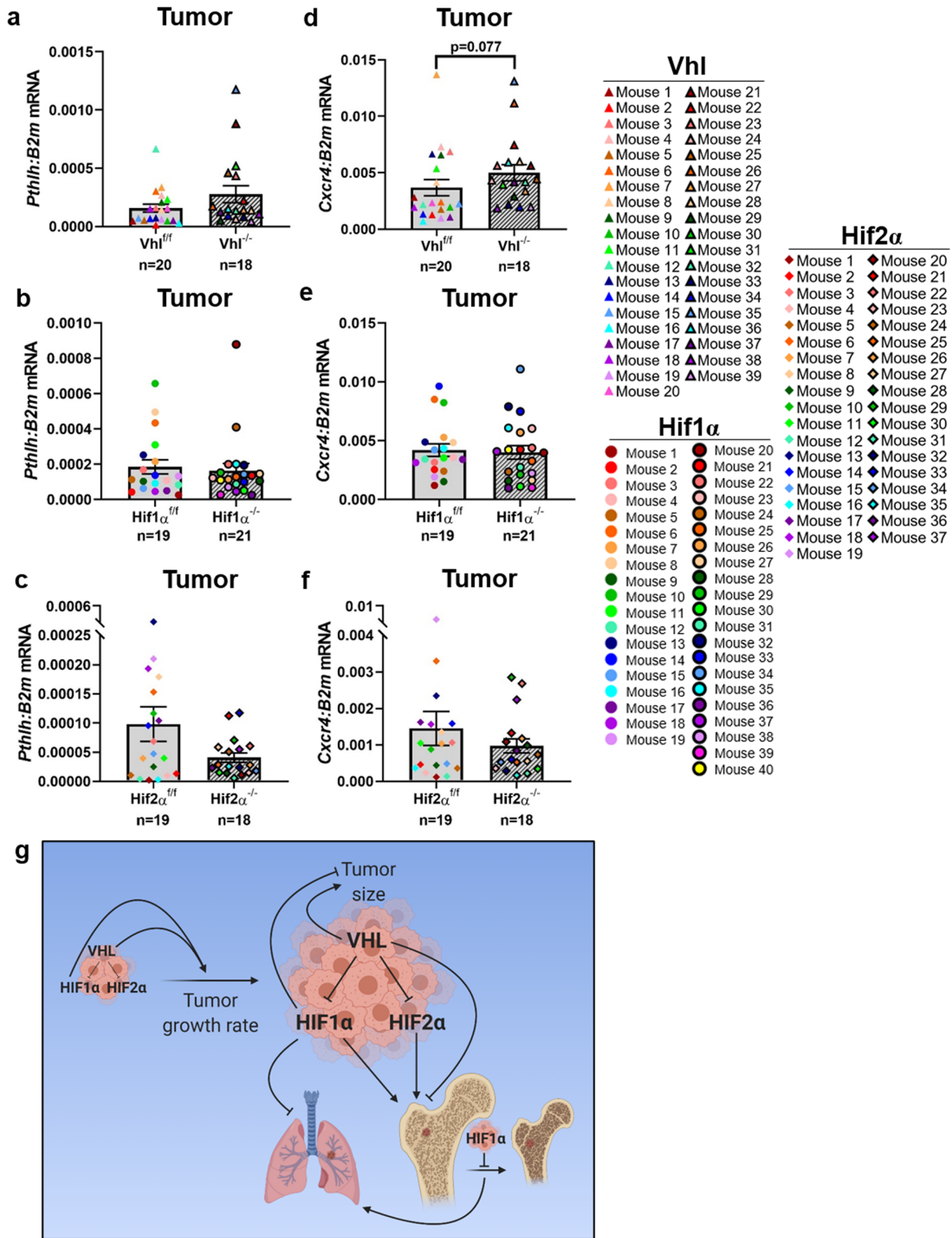


Fig. 7 Deletion of *Vhl* increases tumor dissemination to the bone but not to the lung. **a** Representative 3D renderings of microCT scans of the proximal metaphysis of the right tibia. **b** Quantification of bone volume from microCT analysis as a percentage of total volume. Two-tailed Mann-Whitney test against corresponding *f/f* control. *n* = 10 *Vhl*^{f/f} PyMT⁺ mouse tibiae, *n* = 11 *Vhl*^{-/-} PyMT⁺ mouse tibiae, *n* = 8 *Vhl*^{f/f} PyMT⁻ mouse tibiae, and *n* = 13 *Vhl*^{-/-} PyMT⁻ mouse tibiae. **c** The percentage of EpCAM⁺ cells, out of the total number of live cells, detected by flow cytometric analysis of left hindlimb bone marrow. Values have been normalized to the total tumor burden at end point of each mouse. Two-tailed Mann-Whitney test. *n* = 10 *Vhl*^{f/f} PyMT⁺ mice, *n* = 10 *Vhl*^{-/-} PyMT⁺ mice. **d, e** Quantitative PCR analysis of *Pymt* transcript compared to *Hmbs* from right femur or spinal midsection, respectively. Values have been normalized to the total tumor burden at end point of each mouse. Two-tailed Mann-Whitney test. **f, g** Metastatic lesion number or area detected by histological analysis of H&E-stained sections from the left lung. Values have been normalized to the total tumor burden at end point of each mouse. Two-tailed Mann-Whitney test. **h** Comparison of the proportion of mice from each group that had any detectable pulmonary lesions. Fisher's exact test. **i, j** Quantitative PCR analysis of *Pymt* transcript compared to *B2m* from the right lung or brain, respectively. Values have been normalized to the total tumor burden at end point of each mouse. Two-tailed Mann-Whitney test. Graphs represent mean per group and error bars represent s.e.m. For **d-j**, *n* = 20 (or 19 in **f-h**) *Vhl*^{f/f} PyMT⁺ mice, *n* = 19 *Vhl*^{-/-} PyMT⁺ mice.



regulate HIF signaling activity by modulating degradation of HIF1α and HIF2α, VHL also possesses HIF-independent functions^{80,81}. For example, VHL has been shown to degrade or inhibit the catalytic activity of certain kinases, including some PKC isoforms⁸²⁻⁸⁴, AKT1, and AKT2⁸⁵. These kinases are involved in signaling pathways that regulate metabolism, angiogenesis, proliferation, differentiation, cell survival, tumor

initiation, and metastasis⁸⁶⁻⁸⁸. Thus, it is possible that phenotypes observed in the Vhl^{-/-} PyMT⁺ mice may be due, in part, to these HIF-independent pathways. To definitively address whether the phenotype and potential mechanisms observed in the Vhl^{-/-} mice are specific for Hif1α or Hif2α, loss-of-function Vhl/Hif1α and Vhl/Hif2α double knockout mice will need to be investigated in future studies.

Fig. 8 HIF signaling in the primary tumor drives dissemination to the bone but only modestly alters factors known to regulate bone metastasis.

a–c Quantitative PCR analysis of *Pthlh* transcript compared to *B2m* in primary tumor with deletion of *Vhl*, *Hif1a*, or *Hif2a*, respectively. Two-tailed Mann-Whitney test. **d–f** Quantitative PCR analysis of *Cxcr4* transcript compared to *B2m* in primary tumor with deletion of *Vhl*, *Hif1a*, or *Hif2a*, respectively. Two-tailed Mann-Whitney test. **g** Summary of findings. VHL and HIF1 α expression in the primary tumor drive tumor growth, and VHL expressing tumors are larger, while HIF1 α -expressing tumors are smaller on average. HIF1 α expression in the primary tumor also disrupts bone homeostasis, leading to decreased bone volume. This disruption of the bone inhibits tumor cell dissemination to bone, while likely promoting tumor cell dissemination and outgrowth in the lung. HIF2 α drives bone dissemination but does not influence lung metastasis. As the negative regulator of HIF signaling, VHL inhibits bone metastasis but VHL expression does not alter metastatic tumor burden in the lung. Image created with BioRender.com. Graphs represent mean per group and error bars represent s.e.m. $n = 20$ *Vhl*^{f/f} PyMT⁺ mice, $n = 18$ *Vhl*^{-/-} PyMT⁺ mice, $n = 19$ *Hif1a*^{f/f} PyMT⁺ mice, $n = 21$ *Hif1a*^{-/-} PyMT⁺ mice, $n = 19$ *Hif2a*^{f/f} PyMT⁺ mice, $n = 18$ *Hif2a*^{-/-} PyMT⁺ mice.

Our findings present important considerations for the development of clinical HIF inhibitors. While targeted inhibition of HIF1 α or HIF2 α could be beneficial in preventing bone metastasis, HIF1 α inhibition may promote the outgrowth of lung-disseminated breast cancer cells. Thus, the site-specific effects of tumor cell HIF signaling must be considered. Furthermore, our results suggest that patients with high levels of HIF1 α or HIF2 α expression in their primary tumor may be at an increased risk of bone metastasis development. Thus, these markers may have prognostic value and patients with high expression may benefit from bone-focused clinical follow-up over time.

Methods

Animals. All experiments were performed following the relevant guidelines and regulations of the Animal Welfare Act and the Guide for the Care and Use of Laboratory Animals and were approved by the Institutional Animal Care and Use Committee at Vanderbilt University.

Mammary epithelial tumor cell-specific knock-out of *Hif1a* was achieved by breeding together three transgenic mouse strains. First, transgenic mice with loxP sites flanking both alleles of the *Hif1a* exon 2 (Jackson Laboratory Stock No. 007561, C57/B6 background)⁸⁹ were bred with transgenic mice expressing Cre recombinase downstream of MMTV-LTR (Jackson Laboratory Stock No. 003553, C57/B6 background)⁹⁰. The progeny from this cross were then bred with transgenic mice expressing the PyMT oncoprotein under the MMTV-LTR (Jackson Laboratory Stock No. 022974, C57/B6-FVB mixed background)⁹¹. Virgin female mice with *Hif1a* wild-type mammary fat pad tumors (*Hif1a*^{f/f} PyMT⁺ = *Hif1a*^{f/f}, MMTV-Cre negative, MMTV-PyMT positive) or *Hif1a*-null mammary fat pad tumors (*Hif1a*^{-/-} PyMT⁺ = *Hif1a*^{f/f}, MMTV-Cre positive, MMTV-PyMT positive) were used in these studies. Non-tumor bearing (PyMT⁻) controls of both *Hif1a*^{f/f} and *Hif1a*^{-/-} mice were also used.

Mammary epithelial tumor cell-specific knock-out of *Hif2a* was achieved using the same breeding strategy as above but using a transgenic mouse line with loxP sites flanking both alleles of the *Hif2a* exon 2 (Jackson Laboratory Stock No. 008407, C57/B6 background)⁹². *Hif2a*^{f/f} PyMT⁺ = *Hif2a*^{f/f}, MMTV-Cre negative, MMTV-PyMT positive; *Hif2a*^{-/-} PyMT⁺ = *Hif1a*^{f/f}, MMTV-Cre positive, MMTV-PyMT positive.

Similarly, mammary epithelial tumor cell-specific knock-out of *Vhl* was achieved by incorporating a transgenic mouse line with loxP sites flanking both alleles of the *Vhl* exon 1 (Jackson Laboratory Stock No. 012933, C57/B6 background)⁹³. *Vhl*^{f/f} PyMT⁺ = *Vhl*^{f/f}, MMTV-Cre negative, MMTV-PyMT positive; *Vhl*^{-/-} PyMT⁺ = *Vhl*^{f/f}, MMTV-Cre positive, MMTV-PyMT positive.

At weaning, tail snips were collected from each mouse. Genomic DNA was extracted from the tail snip and genotyping was performed by PCR amplification of *Hif1a* (F: GGAGCTATCTCTAGACC, R: GCAGTTAAGAGCACTAGTTG)⁹⁴, *Hif2a* (F: CTTCTCCATCATCTGGATCTGGGAC, R: CAGGCAGTATGCC TGGCTAATCCAGTT)⁹², or *Vhl* (F: CTAGGCACCGAGCTTAGAGGTTGCG, R: CTGACTCCACTGATGCTGTCCACAG)⁹⁴, as well as *PyMT* (F: GGAA GCAAGTACTTCAACAAGG, R: GGAAAGTCACTAGGAGCAGGG), and *Cre* (F: GCGGTCTGGCAGTAAAACTATC, R: GTGAAACAGCATTGCTGTC ACTT). The *PyMT* genotyping reaction also included an internal positive control reaction (F: CAAATGTTGCTTGTCTGGTG, R: GTCAGTCGAGTGCACAG TTT). Primer sequences for *PyMT* and *Cre* genotyping were obtained from Jackson Laboratories. Once weaned, mice were palpated 2–3 times per week, and tumors were measured in three dimensions with digital calipers. Mice were collected when any tumor had grown to a size of 1 cm in diameter in any dimension, around 4–5 months of age. Littermate and cousin control mice were collected for each study. Forty-five minutes prior to collection, mice were inoculated with Hypoxyprobe (Hypoxyprobe-1 Omni Kit, Hypoxyprobe, Inc., catalog number HP3-1000Kit) via intraperitoneal injection at a dosage of 60 mg/kg body weight.

Real-time PCR. Tumor samples, right lung lobes, brains, and intact right femora were homogenized in 1 ml TRIzol (Life Technologies), spun down to clear the lysate, phenol-chloroform extracted, DNase digested (TURBO DNA-free Kit, Life Technologies), and cDNA synthesized (1 μ g RNA, iScript cDNA Synthesis Kit, Bio-Rad) per the manufacturer's instructions. Real-time PCR was performed using iTaq Universal SYBR Green Supermix (Bio-Rad) on a QuantStudio 5 (Thermo Fisher) with the following conditions: 2 min at 50 °C, 10 min at 95 °C, (15 s at 95 °C, 1 min at 60 °C) \times 40 cycles followed by dissociation curve (15 s at 95 °C, 1 min at 60 °C, 15 s at 95 °C). For each biological replicate, three technical replicates were performed for each gene analyzed. Non-template controls were included as a negative control for each gene analyzed. Analysis was performed by normalizing the expression of the target gene to the average *Hmbs* or *B2m* expression within the same sample to determine Δ Ct. The Δ Ct was transformed ($2^{-\Delta$ Ct}) and the average of the three technical replicates was calculated. The average $2^{-\Delta$ Ct} for each mouse is presented as target gene “(PyMT, *Hif1a*, *Hif2a*, etc.): (*B2m* or *Hmbs*) mRNA” or “Relative mRNA abundance” in the figures. Mouse primers for PyMT⁹⁵ (PyMT—F: CTGCTACTGCACCCAGACAA, R: GCAGGTAAGAGGCATTCTGC) and hydroxymethylbilane synthase⁹⁶ (*Hmbs*—F: TCATGTCCGGTAAACGGCG, R: CACTCGAATCACCCCTCATCTTTG) were previously published. Primer sequences for parathyroid hormone-related protein (*Pthlh*—F: ACATTGTACTGGGAGCCAC, R: TAGGAATCAGCGCCTCTAAC) were kindly provided by Dr. Natalie Sims and Dr. T. John Martin at St. Vincent's Institute of Medical Research. Primers for beta-2-microglobulin, VEGFA, *Hif1a* (exon 2), *Hif2a* (exon 2), and *Vhl* (exon 1) were designed using PrimerBlast (NCBI) against the mouse genome (*Mus musculus*) and validated by dissociation: *B2m* (F: TTCACCCCTCATGAGACTG AT, R: GTCTTGGGCTCGGCCATA), *Vegfa* (F: GGAGATCTCTCGAGGAGCAC TT, R: GCGGATTTAGCAGCAGATATAAGAA), *Hif1a* (F: TCGCGAAGCAA AGAGTCTG, R: GCTCACATTGTGGGGAAGTG), *Hif2a* (F: TGAGGAAGGAG AAATCCCGTG, R: GGGCAACTCATGAGCCAACT), *Vhl* (F: GACCCGTCCA ATAATGCC, R: CGTCGAAGTTGAGCCACAAA). Additional primer sequences were obtained from the Massachusetts General Hospital PrimerBank and specificity was confirmed by nucleotide BLAST (NCBI) and validated by dissociation: *Cdh1* (F: CAGGTCTCCTCATGGCTTTG, R: CTTCCGAAAAGAA GGCTGTCC), *Cdh2* (F: AGCGCAGTCTACCGAAGG, R: TCGCTGCTTTCAT ACTGAACTTT), *Egfr* (F: ATGAAAACCTATGCCTTAGCC, R: TAAGTT CCGATGGGAGTTC), *Notch1* (F: GATGGCTCAATGGGTACAAG, R: TCGTGTGTGTGATGTACAGT), *Snai1* (F: CACACGTCTGCTGTGTCT, R: GCTCAGCAAAAAGCAGGTT), *Snai2* (F: CATCCTTGGGCGTGTAAAGTC, R: GCCAGAGAACGTAGAATAGGTC), *Snai3* (F: GGTCCCAACTACGGG AAAC, R: CTGTAGGGGGTCACTGGGATT), *Twist1* (F: GGACAAGCTG AGCAAGATCCA, R: CGGAGAAGCGGTAGCTGAG), *Zeb1* (F: ACTGCAAG AACGGTTTTCC, R: GCGGAGGAACACTGAGATGT), *Zeb2* (F: ATTGCAC ATCAGACTTTGAGGAA, R: ATAATGGCCGTGTCGCTCG), *Atg7* (F: TCTGGGAAGCCATAAAGTCAG, R: CGCAAGTCCAGGAGCAGAA), *Becn1* (F: ATGGAGGGGTCTAAGGCGTC, R: TCCTCTCCTGAGTTAGCTCT), *Map1lc3a* (F: GACCGCTGTAAGGAGGTGC, R: CTTGACCAACTCGCTCA TGTTA), *Map1lc3b* (F: TTATAGAGCGATACAAGGGGGAG, R: CGCCGTCT GATTATCTTGATGAG), *Sqstm1* (F: GAACTCGCTATAAGTGCAGTGT, R: AGAGAAGCTATCAGAGAGGTGG), *Ulk1* (F: AAGTTCGAGTCTCTCCG AAG, R: CGATGTTTTCGTGCTTATGTTCC), *Pgk1* (F: TGTTGGGTGTGA ATCTGCC, R: ACTTTAGCGCCTCCCAAGATA), *Glut1* (F: CAGTTCGGCTAT AACACTGGT, R: GCCCCGACAGAGAAGATG), *Tek* (F: CTGAGGTT ACTCAAGATGTGAC, R: TCCGTATCCTTATAGCCTGTCC), *Pdgfb* (F: CATCCGCTCCTTTGATGATCTT, R: GTGCTCGGGTCACTGTTCAAGT), *Cxcr4* (F: GAGGCCAAGGAAACTGCTG, R: GCGGTCCAGATGTACCTGTCT). The expression of a panel of metastasis-associated genes was quantified using the tumor metastasis (SAB Target List, M384) qPCR array plate (Bio-Rad). Each gene in the array was run in duplicate. Three representative *Hif1a*^{f/f} and *Hif1a*^{-/-} tumor homogenate RNA samples were selected based on their *Hif1a* expression. Analysis was performed by normalizing the expression of the target gene to the average *B2m* expression within the same sample to determine Δ Ct. The Δ Ct was transformed ($2^{-\Delta$ Ct}) and the average of the two technical replicates was calculated. Δ Ct values for each *Hif1a*^{-/-} sample was then normalized against the average of the three *Hif1a*^{f/f} samples to determine enrichment.

Polymerase chain reaction. Recombination and loss of the *Hif1 α* exon 2 was confirmed by PCR amplification using a three-primer system split between two separate reactions. The forward primer (Fwd: CAGTGCACAGAGCCTCCTC) binds to *Hif1 α* exon 1, the first reverse primer (Rev1: GCTCACATTGTGGG GAAGTG) binds to exon 2, and the second reverse primer (Rev2: ATGTAAAC CATGTGCCCGTC) binds to exon 3. The first reaction (Fwd and Rev1 primers) will not amplify a band if recombination has occurred, while the second reaction (Fwd and Rev2) will amplify a lower molecular weight band in the case of recombination. PCR reactions were set up using the HotStarTaq system (Qiagen) using 200 ng of cDNA generated from RNA extracted from tumor homogenates as the template. PCR reactions were carried out in a T100 Thermal Cycler (Bio-Rad) with the following conditions: 15 min at 95 °C, (1 min at 94 °C, 1.5 min at 59 °C, 1 min at 72 °C) \times 38 cycles, followed by 10 min at 72 °C. The *B2m* locus was also amplified as a loading control, using the same primers as used for real-time PCR above, using the following conditions: 15 min at 95 °C, (1 min at 94 °C, 1.5 min at 53 °C, 1 min at 72 °C) \times 35 cycles, followed by 10 min at 72 °C.

Recombination of *Vhl* exon 1 was confirmed by PCR amplification using a one-reaction three-primer system⁹⁷. The first forward primer (Fwd1: CTGGTACCAC GAAACTGTC) binds to the 3' UTR upstream of *Vhl* exon 1, the second forward primer (Fwd2: CTAGGCACCGAGCTTAGAGGTTTGCG) binds to *Vhl* exon 1, and the reverse primer (Rev: CTGACTTCCACTGATGCTTGTACAG) binds to a region in the first intron. If no recombination has occurred, only one fragment will amplify (Fwd2 and Rev primer pair) since the amplification fragment that would form from the Fwd1 and Rev primer pair is too large to amplify. If recombination has occurred, the binding site for the Fwd2 primer is no longer present, and a lower molecular weight band will form (Fwd1 and Rev primers). PCR reactions were set up using the HotStarTaq system (Qiagen) using 200 ng of cDNA generated from RNA extracted from tumor homogenates as the template. PCR reactions were carried out in a T100 Thermal Cycler (Bio-Rad) with the following conditions: 15 min at 95 °C (1 min at 94 °C, 1.5 min at 52 °C, 1 min at 72 °C) \times 35 cycles, followed by 10 min at 72 °C.

Histology. All tissues collected were fixed in 10% formalin for 24 h. Hind limb bones were then decalcified in EDTA (20% pH 7.4) solution for 72 h prior to embedding. Tissues analyzed via histology and immunohistochemistry were embedded in paraffin and 5 μ m-thick sections were prepared for staining. Hematoxylin and eosin (H&E) staining was performed⁹⁸ and H&E-stained slides of left lung, liver, and tibia sections were analyzed for the presence of metastatic mammary tumors under blinded conditions by a board-certified veterinary anatomic pathologist. All tumors were imaged on an Olympus BX43 microscope equipped with a SPOT Flex camera (Diagnostic Instruments Inc., Sterling Heights, MI). Tumor areas were measured in the SPOT software (Diagnostic Instruments Inc.), and total tumor area per animal was calculated.

Pimonidazole immunohistochemistry. Sections were deparaffinized and rehydrated by soaking the slides in Xylene Substitute (Thermo Fisher), 100, 95, 90, and then 70% ethanol, and finally deionized water. Peroxidase activity was then quenched by incubating the slides in 3% hydrogen peroxide for 15 min. After slowly displacing the hydrogen peroxide solution with deionized water, slides were rinsed three times with phosphate-buffered saline (PBS). The deparaffinized sections were blocked in serum-free protein blocking agent (Dako) for 5 min and incubated with primary antibody (Hypoxyprobe-1 Omni Kit, Hypoxyprobe, Inc., catalog number HP3-1000Kit, 1:100) in Dako protein block overnight at 4 °C. Negative control sections were incubated with Dako alone. The sections were then washed three times with PBS and incubated with biotinylated secondary antibody (goat-anti-rabbit IgG, Vector, catalog number BA-1000, 1:200) in Dako protein block for 30 min at 37 °C, followed by streptavidin-conjugated horseradish peroxidase (HRP; Millipore, OR03L, 1:200) in PBS for 30 min at 37 °C, and developed using the DAB ImmPACT Kit (Vector, catalog number SK-4105) for approximately 1 min. Chromogen development was then quenched by rinsing twice in deionized water. Sections were counterstained with hematoxylin and dehydrated by soaking them in 70, 90, 95, and 100% ethanol, followed by Xylene Substitute. The coverslips were mounted using Permount (Fisher Scientific). All images were collected on an Olympus BX41 Microscope equipped with an Olympus DP71 camera using the \times 4, \times 20, and \times 40 objectives. Pimonidazole-positive tumor area was quantified based on visual inspection of multiple micrographs with \times 4 objective based on a scale of 0–3: 0 = no nuclear staining, 1 = <10% positive nuclear staining, 2 = 10–50% positive nuclear staining, 3 = \geq 50% positive nuclear staining. Each field was assigned a score and an average score for the tumor was calculated based on all fields. The number of fields inspected varied from 1 to 4, depending on the size of the tumor. Pimonidazole-stained area of lung lesions was quantified using the ImageJ software with manual tumor area contouring and automatic color thresholding.

Ki-67 immunohistochemistry. Staining was performed by the Vanderbilt University Medical Center Translational Pathology Shared Resource (Nashville, TN) as follows: Slides were placed on the Leica Bond Max IHC stainer. All steps besides dehydration, clearing, and coverslipping are performed on the Bond Max. Slides are deparaffinized. Heat-induced antigen retrieval was performed on the Bond Max

using their Epitope Retrieval 2 solution for 20 min. Slides were placed in a Protein Block (Ref# x0909, DAKO, Carpinteria, CA) for 10 min. The sections were incubated with anti-Ki-67 (Catalog #12202 S, Cell Signaling Technology, Danvers, MA) diluted 1:250 for 1 h. The Bond Refine Polymer detection system was used for visualization. Slides were dehydrated, cleared, and coverslipped. All images were collected on an Olympus BX41 Microscope equipped with an Olympus DP71 camera using the \times 4, \times 20, and \times 40 objectives. Ki-67-stained area of lung lesions was quantified using the ImageJ software with manual tumor area contouring and automatic color thresholding.

CD4/CD8 immunofluorescent imaging. Slides were stained using the Opal 7-Color Manual IHC Kit (PerkinElmer). In brief, slides were deparaffinized and rehydrated in a series of xylene and ethanol washes, microwaved in Rodent Decloaker (Biocare Medical), and then cooled. Slides were washed with water and then TBST (TBS + 0.05% Tween-20) followed by blocking with BLOXALL Blocking Solution (Vector Laboratories). The following antibodies were used: CD4 (Invitrogen, clone 4SM95; 1:100), CD8 (Invitrogen, clone 4SM16; 1:100), ImmPRESS HRP Goat anti-rat IgG (Vector Laboratories; 1:4). Staining with primary and secondary antibodies and OPAL fluorophores were performed per the manufacturer's instructions. All images were collected on a Zeiss 880/Airyscan Microscope using the \times 20 and \times 40 objectives. For quantitation, the \times 20 images were used to manually count the number of CD4⁺ and CD8⁺ cells and calculate nuclear area using color thresholding in ImageJ.

Microcomputed tomography. Ex vivo microCT was performed on the proximal tibia using the Scanco μ CT 50. Scans were initiated from the proximal end of the metaphyseal growth plate and progressed 250 slices distal. Tibiae were scanned at 7 μ m voxel resolution, 55-kV voltage, and 200 μ A current. Scans were reconstructed and analyzed using the Scanco Medical Imaging Software to determine the bone volume/total volume, trabecular number, thickness, and separation. The most distal slice of the growth plate was used as a reference slice and analysis was set to begin 20 slices distal from this point. A 150 slice region of interest was selected for analysis. An automated contouring procedure was applied to separate the trabecular bone from the cortical bone and visually verified for each sample.

Flow cytometry. The epiphyses of the femur and tibia from one hindlimb were cut and the bones were flushed using centrifugation to obtain the bone marrow. The bone marrow was filtered through a 40 μ m cell strainer to separate the cells from bone debris. Cells were suspended in red blood cell lysis buffer for 5 min on ice, spun down, and washed twice with PBS. Bone marrow (2×10^6 cells) was stained in 100 μ l of 1% bovine serum albumin in PBS with 100 ng EpCAM antibody (BD Pharmingen, catalog number 563478) for 1 h at 4 °C in the dark. Cells were washed with PBS and resuspended in PBS and 0.5 ng 4,6-diamidino-2-phenylindole (DAPI) for 15 min on ice. Flow cytometric experiments were analyzed in the VUMC Flow Cytometry Shared Resource using the 3-laser or 5-laser BD LSRII. Datasets were analyzed using the FlowJo software (FlowJo, LLC). Cells were gated based on forward scatter and side scatter to identify single cells and then live cells (DAPI⁻) were gated based on EpCAM positivity using non-tumor-bearing bone marrow as a negative control. Mammary fat pad tumors were mechanically digested and filtered through a 40 μ m cell strainer to obtain a single-cell suspension. These tumor cells were stained as described above and used as a positive control.

TCGA patient data analysis. The Cancer Genome Atlas cBioPortal^{99,100} was accessed on 16 November 2020, 17 November 2020, and 15 April 2021 to determine whether the hypoxia gene signature⁴⁵ from $n = 1100$ patients with Breast Invasive Carcinoma (Firehose Legacy dataset; http://www.cbioportal.org/study/summary?id=brca_tcga) correlated with bone⁴⁶ and lung metastasis signatures⁴⁷. Genes from the hypoxia, bone metastasis, and lung metastasis gene signatures were entered into the query gene field for cBioPortal separately. The mRNA expression (RNA Seq V2 RSEM) for each gene across all 1100 patients was downloaded and saved in Excel format. For each gene in the three gene signatures, the gene expression provided by RNAseq was normalized to the median expression of that gene across all patients¹⁰¹. We next averaged the expression score for all of the genes in that signature for each individual patient. A log conversion was applied to the normalized, averaged gene signature expression scores. These signature scores were plotted against each other as a correlation graph in the Prism software (Graphpad) with a linear regression curve.

Statistics and reproducibility. To calculate sample size, we previously consulted with a biostatistician within the Department of Radiation Oncology at Stanford University who performed power calculations. The power calculations were based on previously published in vivo studies³³. For the transgenic mouse lines, a sample size of $n = 10$ mice/group will provide 85% power in a two-sided t test with an alpha level 0.05 with a variation of 8.5 and an expected difference of 12. Thus, we sought to collect a minimum of $n = 10$ mice/group to ensure adequate statistical analysis at end point for these experiments. For all studies, n per group is as indicated in the figure or figure legend and the scatter dot plots indicate the mean of each group and the standard error of the mean. All graphs and statistical analyses were generated using the Prism software (Graphpad). All in vitro and in vivo assays were analyzed for statistical significance using two-tailed

Mann–Whitney test, log-rank test, or Fisher’s exact test, as denoted in figure legends. Pearson and Spearman correlation coefficients were calculated for gene signature correlation analyses. $P < 0.05$ was statistically significant.

Reporting summary. Further information on research design is available in the Nature Research Reporting Summary linked to this article.

Data availability

Raw data underlying figures can be found in Supplementary Data 1. Unedited DNA gel images are available in the Supplementary Information (Supplementary Figs. 7–12). Any other data that support the findings of this study are available from the corresponding author, R.W.J. upon reasonable request.

Received: 17 February 2021; Accepted: 8 September 2021;

Published online: 23 September 2021

References

- Nakazawa, M. S., Keith, B. & Simon, M. C. Oxygen availability and metabolic adaptations. *Nat. Rev. Cancer* **16**, 663–673 (2016).
- Semenza, G. L. & Wang, G. L. A nuclear factor induced by hypoxia via de novo protein synthesis binds to the human erythropoietin gene enhancer at a site required for transcriptional activation. *Mol. Cell Biol.* **12**, 5447–5454 (1992).
- Wang, G. L., Jiang, B. H., Rue, E. A. & Semenza, G. L. Hypoxia-inducible factor 1 is a basic-helix-loop-helix-PAS heterodimer regulated by cellular O₂ tension. *Proc. Natl Acad. Sci. USA* **92**, 5510–5514 (1995).
- Tian, H., McKnight, S. L. & Russell, D. W. Endothelial PAS domain protein 1 (EPAS1), a transcription factor selectively expressed in endothelial cells. *Genes Dev.* **11**, 72–82 (1997).
- Gu, Y. Z., Moran, S. M., Hogensch, J. B., Wartman, L. & Bradfield, C. A. Molecular characterization and chromosomal localization of a third alpha-class hypoxia inducible factor subunit, HIF3alpha. *Gene Expr.* **7**, 205–213 (1998).
- Gossage, L., Eisen, T. & Maher, E. R. VHL, the story of a tumour suppressor gene. *Nat. Rev. Cancer* **15**, 55–64 (2015).
- Huang, L. E., Gu, J., Schau, M. & Bunn, H. F. Regulation of hypoxia-inducible factor 1alpha is mediated by an O₂-dependent degradation domain via the ubiquitin-proteasome pathway. *Proc. Natl Acad. Sci. USA* **95**, 7987–7992 (1998).
- Ohh, M. et al. Ubiquitination of hypoxia-inducible factor requires direct binding to the beta-domain of the von Hippel-Lindau protein. *Nat. Cell Biol.* **2**, 423–427 (2000).
- Tanimoto, K., Makino, Y., Pereira, T. & Poellinger, L. Mechanism of regulation of the hypoxia-inducible factor-1 alpha by the von Hippel-Lindau tumor suppressor protein. *EMBO J.* **19**, 4298–4309 (2000).
- Ivan, M. et al. HIF1alpha targeted for VHL-mediated destruction by proline hydroxylation: implications for O₂ sensing. *Science* **292**, 464–468 (2001).
- Jaakkola, P. et al. Targeting of HIF-1alpha to the von Hippel-Lindau ubiquitylation complex by O₂-regulated prolyl hydroxylation. *Science* **292**, 468–472 (2001).
- Schodel, J. et al. High-resolution genome-wide mapping of HIF-binding sites by CHIP-seq. *Blood* **117**, e207–e217 (2011).
- Mole, D. R. et al. Genome-wide association of hypoxia-inducible factor (HIF)-1alpha and HIF-2alpha DNA binding with expression profiling of hypoxia-inducible transcripts. *J. Biol. Chem.* **284**, 16767–16775 (2009).
- Xia, X. & Kung, A. L. Preferential binding of HIF-1 to transcriptionally active loci determines cell-type specific response to hypoxia. *Genome Biol.* **10**, R113 (2009).
- Shweiki, D., Itin, A., Soffer, D. & Keshet, E. Vascular endothelial growth factor induced by hypoxia may mediate hypoxia-initiated angiogenesis. *Nature* **359**, 843–845 (1992).
- Tsuzuki, Y. et al. Vascular endothelial growth factor (VEGF) modulation by targeting hypoxia-inducible factor-1alpha-> hypoxia response element-> VEGF cascade differentially regulates vascular response and growth rate in tumors. *Cancer Res.* **60**, 6248–6252 (2000).
- Firth, J. D., Ebert, B. L. & Ratcliffe, P. J. Hypoxic regulation of lactate dehydrogenase A. Interaction between hypoxia-inducible factor 1 and cAMP response elements. *J. Biol. Chem.* **270**, 21021–21027 (1995).
- Gleadle, J. M. & Ratcliffe, P. J. Induction of hypoxia-inducible factor-1, erythropoietin, vascular endothelial growth factor, and glucose transporter-1 by hypoxia: evidence against a regulatory role for Src kinase. *Blood* **89**, 503–509 (1997).
- Firth, J. D., Ebert, B. L., Pugh, C. W. & Ratcliffe, P. J. Oxygen-regulated control elements in the phosphoglycerate kinase 1 and lactate dehydrogenase A genes: similarities with the erythropoietin 3' enhancer. *Proc. Natl Acad. Sci. USA* **91**, 6496–6500 (1994).
- Ebert, B. L., Firth, J. D. & Ratcliffe, P. J. Hypoxia and mitochondrial inhibitors regulate expression of glucose transporter-1 via distinct Cis-acting sequences. *J. Biol. Chem.* **270**, 29083–29089 (1995).
- Courtney, R. et al. Cancer metabolism and the Warburg effect: the role of HIF-1 and PI3K. *Mol. Biol. Rep.* **42**, 841–851 (2015).
- Petrella, B. L., Lohi, J. & Brinckerhoff, C. E. Identification of membrane type-1 matrix metalloproteinase as a target of hypoxia-inducible factor-2 alpha in von Hippel-Lindau renal cell carcinoma. *Oncogene* **24**, 1043–1052 (2005).
- Erler, J. T. et al. Lysyl oxidase is essential for hypoxia-induced metastasis. *Nature* **440**, 1222–1226 (2006).
- Yang, M. H. et al. Direct regulation of TWIST by HIF-1alpha promotes metastasis. *Nat. Cell Biol.* **10**, 295–305 (2008).
- Schindl, M. et al. Overexpression of hypoxia-inducible factor 1alpha is associated with an unfavorable prognosis in lymph node-positive breast cancer. *Clin. Cancer Res.* **8**, 1831–1837 (2002).
- Dales, J. P. et al. Overexpression of hypoxia-inducible factor HIF-1alpha predicts early relapse in breast cancer: retrospective study in a series of 745 patients. *Int. J. Cancer* **116**, 734–739 (2005).
- Bos, R. et al. Levels of hypoxia-inducible factor-1alpha independently predict prognosis in patients with lymph node negative breast carcinoma. *Cancer* **97**, 1573–1581 (2003).
- Generali, D. et al. Hypoxia-inducible factor-1alpha expression predicts a poor response to primary chemoendocrine therapy and disease-free survival in primary human breast cancer. *Clin. Cancer Res.* **12**, 4562–4568 (2006).
- Cox, T. R. et al. The hypoxic cancer secretome induces pre-metastatic bone lesions through lysyl oxidase. *Nature* **522**, 106–110 (2015).
- Woelfle, U. et al. Molecular signature associated with bone marrow micrometastasis in human breast cancer. *Cancer Res.* **63**, 5679–5684 (2003).
- Fallah, J. & Rini, B. I. HIF inhibitors: status of current clinical development. *Curr. Oncol. Rep.* **21**, 6 (2019).
- Hosseini, H. et al. Early dissemination seeds metastasis in breast cancer. *Nature* **540**, 552–558 (2016).
- Husemann, Y. et al. Systemic spread is an early step in breast cancer. *Cancer Cell* **13**, 58–68 (2008).
- Jin, L. et al. Breast cancer lung metastasis: molecular biology and therapeutic implications. *Cancer Biol. Ther.* **19**, 858–868 (2018).
- Johnson, R. W., Schipani, E. & Giaccia, A. J. HIF targets in bone remodeling and metastatic disease. *Pharmacol. Ther.* **150**, 169–177 (2015).
- Liao, D., Corle, C., Seagroves, T. N. & Johnson, R. S. Hypoxia-inducible factor-1alpha is a key regulator of metastasis in a transgenic model of cancer initiation and progression. *Cancer Res.* **67**, 563–572 (2007).
- Lu, X. et al. In vivo dynamics and distinct functions of hypoxia in primary tumor growth and organotropic metastasis of breast cancer. *Cancer Res.* **70**, 3905–3914 (2010).
- Hiraga, T., Kizaka-Kondoh, S., Hirota, K., Hiraoka, M. & Yoneda, T. Hypoxia and hypoxia-inducible factor-1 expression enhance osteolytic bone metastases of breast cancer. *Cancer Res.* **67**, 4157–4163 (2007).
- Dunn, L. K. et al. Hypoxia and TGF-beta drive breast cancer bone metastases through parallel signaling pathways in tumor cells and the bone microenvironment. *PLoS ONE* **4**, e6896 (2009).
- Sowder, M. E. & Johnson, R. W. Enrichment and detection of bone disseminated tumor cells in models of low tumor burden. *Sci. Rep.* **8**, 14299 (2018).
- Guy, C. T., Cardiff, R. D. & Muller, W. J. Induction of mammary tumors by expression of polyomavirus middle T oncogene: a transgenic mouse model for metastatic disease. *Mol. Cell Biol.* **12**, 954–961 (1992).
- Fantozzi, A. & Christofori, G. Mouse models of breast cancer metastasis. *Breast Cancer Res.* **8**, 212 (2006).
- Dower, C. M., Bhat, N., Wang, E. W. & Wang, H. G. Selective reversible inhibition of autophagy in hypoxic breast cancer cells promotes pulmonary metastasis. *Cancer Res.* **77**, 646–657 (2017).
- Vera-Ramirez, L., Vodnala, S. K., Nini, R., Hunter, K. W. & Green, J. E. Autophagy promotes the survival of dormant breast cancer cells and metastatic tumour recurrence. *Nat. Commun.* **9**, 1944 (2018).
- Ye, I. C. et al. Molecular portrait of hypoxia in breast cancer: a prognostic signature and novel HIF-regulated genes. *Mol. Cancer Res.* **16**, 1889–1901 (2018).
- Kang, Y. et al. A multigenic program mediating breast cancer metastasis to bone. *Cancer Cell* **3**, 537–549 (2003).
- Minn, A. J. et al. Genes that mediate breast cancer metastasis to lung. *Nature* **436**, 518–524 (2005).
- Fluegen, G. et al. Phenotypic heterogeneity of disseminated tumour cells is preset by primary tumour hypoxic microenvironments. *Nat. Cell Biol.* **19**, 120–132 (2017).
- Erler, J. T. et al. Hypoxia-induced lysyl oxidase is a critical mediator of bone marrow cell recruitment to form the premetastatic niche. *Cancer Cell* **15**, 35–44 (2009).
- Keith, B., Johnson, R. S. & Simon, M. C. HIF1alpha and HIF2alpha: sibling rivalry in hypoxic tumour growth and progression. *Nat. Rev. Cancer* **12**, 9–22 (2011).

51. Li, J. et al. PTHrP drives breast tumor initiation, progression, and metastasis in mice and is a potential therapy target. *J. Clin. Invest.* **121**, 4655–4669 (2011).
52. Kiriya, T. et al. Transforming growth factor beta stimulation of parathyroid hormone-related protein (PTHrP): a paracrine regulator? *Mol. Cell Endocrinol.* **92**, 55–62 (1993).
53. Yin, J. J. et al. TGF-beta signaling blockade inhibits PTHrP secretion by breast cancer cells and bone metastases development. *J. Clin. Invest.* **103**, 197–206 (1999).
54. Sterling, J. A., Edwards, J. R., Martin, T. J. & Mundy, G. R. Advances in the biology of bone metastasis: how the skeleton affects tumor behavior. *Bone* **48**, 6–15 (2011).
55. Manisterski, M., Golan, M., Amir, S., Weisman, Y. & Mabeesh, N. J. Hypoxia induces PTHrP gene transcription in human cancer cells through the HIF-2alpha. *Cell Cycle* **9**, 3723–3729 (2010).
56. Guo, F. et al. CXCL12/CXCR4: a symbiotic bridge linking cancer cells and their stromal neighbors in oncogenic communication networks. *Oncogene* **35**, 816–826 (2016).
57. Masuda, T. et al. ANGPTL2 increases bone metastasis of breast cancer cells through enhancing CXCR4 signaling. *Sci. Rep.* **5**, 9170 (2015).
58. Seagroves, T. N. et al. VHL deletion impairs mammary alveologenesis but is not sufficient for mammary tumorigenesis. *Am. J. Pathol.* **176**, 2269–2282 (2010).
59. Parker, K. D., Albeke, S. E., Gigley, J. P., Goldstein, A. M. & Ward, N. L. Microbiome composition in both wild-type and disease model mice is heavily influenced by mouse facility. *Front. Microbiol.* **9**, 1598 (2018).
60. Fessler, J., Matson, V. & Gajewski, T. F. Exploring the emerging role of the microbiome in cancer immunotherapy. *J. Immunother. Cancer* **7**, 108 (2019).
61. Gopalakrishnan, V., Helmink, B. A., Spencer, C. N., Reuben, A. & Wargo, J. A. The influence of the gut microbiome on cancer, immunity, and cancer immunotherapy. *Cancer Cell* **33**, 570–580 (2018).
62. Champy, M. F. et al. Mouse functional genomics requires standardization of mouse handling and housing conditions. *Mamm. Genome* **15**, 768–783 (2004).
63. Zhang, H. et al. HIF-1-dependent expression of angiopoietin-like 4 and L1CAM mediates vascular metastasis of hypoxic breast cancer cells to the lungs. *Oncogene* **31**, 1757–1770 (2012).
64. Goto, Y. et al. UCHL1 provides diagnostic and antimetastatic strategies due to its deubiquitinating effect on HIF-1alpha. *Nat. Commun.* **6**, 6153 (2015).
65. Wong, C. C. et al. Hypoxia-inducible factor 1 is a master regulator of breast cancer metastatic niche formation. *Proc. Natl Acad. Sci. USA* **108**, 16369–16374 (2011).
66. Dunn, G. P., Old, L. J. & Schreiber, R. D. The immunobiology of cancer immunosurveillance and immunoediting. *Immunity* **21**, 137–148 (2004).
67. Andrews, L. P., Yano, H. & Vignali, D. A. A. Inhibitory receptors and ligands beyond PD-1, PD-L1 and CTLA-4: breakthroughs or backups. *Nat. Immunol.* **20**, 1425–1434 (2019).
68. Mantovani, A., Marchesi, F., Malesci, A., Laghi, L. & Allavena, P. Tumour-associated macrophages as treatment targets in oncology. *Nat. Rev. Clin. Oncol.* **14**, 399–416 (2017).
69. Sceneay, J. et al. Primary tumor hypoxia recruits CD11b+/Ly6Cmed/Ly6G+ immune suppressor cells and compromises NK cell cytotoxicity in the premetastatic niche. *Cancer Res.* **72**, 3906–3911 (2012).
70. Reynaud, C. et al. Lysyl oxidase is a strong determinant of tumor cell colonization in bone. *Cancer Res.* **77**, 268–278 (2017).
71. Deep, G. et al. Exosomes secreted by prostate cancer cells under hypoxia promote matrix metalloproteinases activity at pre-metastatic niches. *Mol. Carcinog.* **59**, 323–332 (2020).
72. Wang, H. et al. The osteogenic niche promotes early-stage bone colonization of disseminated breast cancer cells. *Cancer Cell* **27**, 193–210 (2015).
73. Yu-Lee, L. Y. et al. Osteoblast-secreted factors mediate dormancy of metastatic prostate cancer in the bone via activation of the TGFbetaRIII-p38MAPK-pS249/T252RB pathway. *Cancer Res.* **78**, 2911–2924 (2018).
74. Yu-Lee, L. Y. et al. Bone secreted factors induce cellular quiescence in prostate cancer cells. *Sci. Rep.* **9**, 18635 (2019).
75. Martin, T. J. & Johnson, R. W. Multiple actions of parathyroid hormone-related protein in breast cancer bone metastasis. *Br. J. Pharmacol.* <https://doi.org/10.1111/bph.14709> (2019).
76. Fleming, N. I. et al. Parathyroid hormone-related protein protects against mammary tumor emergence and is associated with monocyte infiltration in ductal carcinoma in situ. *Cancer Res.* **69**, 7473–7479 (2009).
77. Henderson, M. et al. Parathyroid hormone-related protein production by breast cancers, improved survival, and reduced bone metastases. *J. Natl Cancer Inst.* **93**, 234–237 (2001).
78. Henderson, M. A. et al. Parathyroid hormone-related protein localization in breast cancers predict improved prognosis. *Cancer Res.* **66**, 2250–2256 (2006).
79. Micucci, C., Matachione, G., Valli, D., Orciari, S. & Catalano, A. HIF2alpha is involved in the expansion of CXCR4-positive cancer stem-like cells in renal cell carcinoma. *Br. J. Cancer* **113**, 1178–1185 (2015).
80. Zhang, J. & Zhang, Q. VHL and hypoxia signaling: beyond HIF in cancer. *Biomedicines.* <https://doi.org/10.3390/biomedicines6010035> (2018).
81. Minervini, G., Pennuto, M. & Tosatto, S. C. E. The pVHL neglected functions, a tale of hypoxia-dependent and -independent regulations in cancer. *Open Biol.* **10**, 200109 (2020).
82. Okuda, H. et al. The von Hippel-Lindau tumor suppressor protein mediates ubiquitination of activated atypical protein kinase C. *J. Biol. Chem.* **276**, 43611–43617 (2001).
83. Iturrioz, X. et al. The von Hippel-Lindau tumour-suppressor protein interaction with protein kinase Cdelta. *Biochem. J.* **397**, 109–120 (2006).
84. Pal, S., Claffey, K. P., Dvorak, H. F. & Mukhopadhyay, D. The von Hippel-Lindau gene product inhibits vascular permeability factor/vascular endothelial growth factor expression in renal cell carcinoma by blocking protein kinase C pathways. *J. Biol. Chem.* **272**, 27509–27512 (1997).
85. Guo, J. et al. pVHL suppresses kinase activity of Akt in a proline-hydroxylation-dependent manner. *Science* **353**, 929–932 (2016).
86. Gould, C. M. & Newton, A. C. The life and death of protein kinase C. *Curr. Drug Targets* **9**, 614–625 (2008).
87. Newton, A. C. Protein kinase C: poised to signal. *Am. J. Physiol. Endocrinol. Metab.* **298**, E395–E402 (2010).
88. Hinz, N. & Jucker, M. Distinct functions of AKT isoforms in breast cancer: a comprehensive review. *Cell Commun. Signal* **17**, 154 (2019).
89. Ryan, H. E. et al. Hypoxia-inducible factor-1alpha is a positive factor in solid tumor growth. *Cancer Res.* **60**, 4010–4015 (2000).
90. Wagner, K. U. et al. Cre-mediated gene deletion in the mammary gland. *Nucleic Acids Res.* **25**, 4323–4330 (1997).
91. Davie, S. A. et al. Effects of FVB/NJ and C57Bl/6J strain backgrounds on mammary tumor phenotype in inducible nitric oxide synthase deficient mice. *Transgenic Res.* **16**, 193–201 (2007).
92. Gruber, M. et al. Acute postnatal ablation of Hif-2alpha results in anemia. *Proc. Natl Acad. Sci. USA* **104**, 2301–2306 (2007).
93. Haase, V. H., Glickman, J. N., Socolovsky, M. & Jaenisch, R. Vascular tumors in livers with targeted inactivation of the von Hippel-Lindau tumor suppressor. *Proc. Natl Acad. Sci. USA* **98**, 1583–1588 (2001).
94. Biju, M. P. et al. Vhlh gene deletion induces Hif-1-mediated cell death in thymocytes. *Mol. Cell Biol.* **24**, 9038–9047 (2004).
95. Smith, B. A. et al. Targeting the PyMT oncogene to diverse mammary cell populations enhances tumor heterogeneity and generates rare breast cancer subtypes. *Genes Cancer* **3**, 550–563 (2012).
96. Johnson, R. W. et al. The primary function of gp130 signaling in osteoblasts is to maintain bone formation and strength, rather than promote osteoclast formation. *J. Bone Min. Res.* **29**, 1492–1505 (2014).
97. Rankin, E. B. et al. Inactivation of the arylhydrocarbon receptor nuclear translocator (Arnt) suppresses von Hippel-Lindau disease-associated vascular tumors in mice. *Mol. Cell Biol.* **25**, 3163–3172 (2005).
98. Johnson, R. W. et al. TGF-beta promotion of Gli2-induced expression of parathyroid hormone-related protein, an important osteolytic factor in bone metastasis, is independent of canonical Hedgehog signaling. *Cancer Res.* **71**, 822–831 (2011).
99. Cerami, E. et al. The cBio cancer genomics portal: an open platform for exploring multidimensional cancer genomics data. *Cancer Discov.* **2**, 401–404 (2012).
100. Gao, J. et al. Integrative analysis of complex cancer genomics and clinical profiles using the cBioPortal. *Sci. Signal* **6**, pii (2013).
101. Li, B. et al. Fructose-1,6-bisphosphatase opposes renal carcinoma progression. *Nature* **513**, 251–255 (2014).

Acknowledgements

The authors wish to thank Mr. Joshua Johnson for bone histological processing, sectioning, and H&E staining. V.M.T. and R.W.J. are supported by NIH award R00CA194198 (to R.W.J.), and L.A.V., M.E.C., and R.W.J. are supported by DoD Breakthrough Award W81XWH-18-1-0029 (to R.W.J.). M.R. is supported by NIH award R00CA201304. This project was supported in part by scholarship funds from the NIH award P30CA068485 Vanderbilt-Ingram Cancer Center Support Grant, which also supports the Translational Pathology Shared Resource. Flow Cytometry experiments were performed in the VMC Flow Cytometry Shared Resource, which is supported by P30CA68485 and the Vanderbilt Digestive Disease Research Center (DK058404). The results shown here are in part based on data generated by the TCGA Research Network: <https://www.cancer.gov/tcga>.

Author contributions

R.W.J. and V.M.T. conceived the original idea. M.R. provided support and critical feedback to the project and manuscript. R.W.J. supervised the project and provided funding. V.M.T. designed and performed the majority of experiments and data analysis and wrote the manuscript. L.A.V. maintained animal colonies and performed the majority of the animal collections. K.P.S. and C.D.O. performed experiments and assisted V.M.T. L.H. and C.P. performed the lung and liver histology analysis. M.E.C. performed the immunofluorescence experiments and analysis.

Competing interests

The authors declare no competing interests.

Additional information

Supplementary information The online version contains supplementary material available at <https://doi.org/10.1038/s42003-021-02648-3>.

Correspondence and requests for materials should be addressed to Rachelle W. Johnson.

Peer review information *Communications Biology* thanks the anonymous reviewers for their contribution to the peer review of this work. Primary handling editors: Ruby Huang and Eve Rogers. Peer reviewer reports are available.

Reprints and permission information is available at <http://www.nature.com/reprints>

Publisher's note Springer Nature remains neutral with regard to jurisdictional claims in published maps and institutional affiliations.



Open Access This article is licensed under a Creative Commons Attribution 4.0 International License, which permits use, sharing, adaptation, distribution and reproduction in any medium or format, as long as you give appropriate credit to the original author(s) and the source, provide a link to the Creative Commons license, and indicate if changes were made. The images or other third party material in this article are included in the article's Creative Commons license, unless indicated otherwise in a credit line to the material. If material is not included in the article's Creative Commons license and your intended use is not permitted by statutory regulation or exceeds the permitted use, you will need to obtain permission directly from the copyright holder. To view a copy of this license, visit <http://creativecommons.org/licenses/by/4.0/>.

© The Author(s) 2021